www.sciencemag.org/content/361/6403/672/suppl/DC1

Supplementary Materials for

Collective clog control: Optimizing traffic flow in confined biological and robophysical excavation

J. Aguilar*, D. Monaenkova*, V. Linevich, W. Savoie, B. Dutta, H.-S. Kuan, M. D. Betterton, M. A. D. Goodisman, D. I. Goldman†

*These authors contributed equally to this work.
†Corresponding author. Email: daniel.goldman@physics.gatech.edu

Published 17 August 2018, *Science* **361**, 672 (2018)
DOI: 10.1126/science.aan3891

This PDF file includes:

Materials and Methods
Figs. S1 to S26
Tables S1 to S4
Captions for Movies S1 to S5
References

Other Supporting Online Material for this manuscript includes the following:
(available at www.sciencemag.org/content/361/6403/672/suppl/DC1)

Movies S1 to S5

Materials and Methods

1. Ant Experiments

Ten *S. invicta* nests were collected during the spring, summer and autumn of 2014, 2015 and 2016 at the Research and Education Garden of the University of Georgia, GA, USA, and the Chattahoochee-Oconee National Forest, GA, USA. Nest collection and colony extraction were performed according to methods found in (*35*). Ants were housed in plastic bins for 2–3 months at an ambient room temperature of 23±3°C with a relative humidity of 30±2%, and fed *Vespula* larvae and supplied with tap water twice a week.

1.1 Primary Ant Digging Experiments

Small groups of 30 ant workers from the laboratory-housed colonies were isolated in transparent containers filled with simulated cohesive soil made of 0.25 mm diameter wetted glass spheres (Ballotini glass particles). The experiments were conducted for 48 hours in W=0.01 and W=0.1 wet soils (3 trials for each soil moisture). All the experiments were repeated for 3 different colonies. The abdomens of the workers were marked in different colors. A plastic insert separated ants from cohesive soil and featured a single entry point next to the transparent wall of the container. A small (~ 5 mm) indentation was made next to the transparent wall of the container to prompt excavation. In each experiment, ants constructed a single tunnel. The top portion of the container was used by the ants for excavated soil deposition.

The container was fixed on the motorized stage and the camera was focused on the first 2 cm of the tunnel at a distance of approximately 3 ant body lengths. As the tunnel grew in length, the relative positions of the tunnel and the camera were adjusted such that the tip of the tunnel was always visible. The camera was streamed, during which real-time processing detected the presence of ants based on pixel intensity. When an ant entered the camera's field of view, the camera was triggered to record 60 seconds of video at 15 fps.

Work among excavators was characterized by manually counting the number of occurrences in which an ant visited the tunnel. Ants were classified as visitors if they appeared within the camera's view of the tunnel at any point within the duration of the experiment. Non-visitors were those ants that were never detected by the camera. Lorenz curves described the workload distribution by linking the cumulative share of visiting workers in the population (ranged from the least to the most hardworking individuals) to the cumulative share of work performed by the excavating group.

The Gini coefficient (a measure of statistics dispersion) (*15*) derived from the shape of the curve reflected the inequality in the workload distribution within visiting group. In general, when the Gini coefficient is close to 0, the effort of the ants during the excavation is nearly equal. In contrast, a Gini coefficient close to 1 indicates highly unequal workload distribution with a few active diggers in the visiting group carrying out the bulk of the workload. To calculate the Lorenz curves and Gini coefficients of the 48-hour experiments, the only ants that were included were those that were detected as having visited at least once during those 48 hours. To calculate the Lorenz curves and Gini coefficients for 12-hour epochs within those 48-hour experiments, we only considered the ants that visited within those 12-hour time-frames. This ensured that the calculated workload distributions only ever considered the working population of that measured time-period. Note that visitors, which did not successfully dig and reversed without a pellet were also counted in the excavation effort, because non-excavating visitors still expend energy in an excavation attempt and contribute to tunnel traffic. The 48 hour experiments revealed no significant effects of epoch (1-way ANOVA $F_{3, 20}$=0.85, p=0.48) or soil wetness W (1-way ANOVA, $F_{1, 23}$=2.54, p=0.13) on the Gini coefficients obtained from Lorenz curves. Similar workload inequality characteristics are observed from the first 3 hours, by which point the tunnel length has typically not yet exceeded 2 cm. A summary of Gini coefficients extracted from the experiment is provided in Table S1.

1.2 Active Removal Ant Experiment

To determine how the removal of top 5 most active diggers from the colony affects the workload distribution and efficiency of tunnel construction, groups of 30 ants were set to excavate cohesive granular media. Rarely, an ant would lose its colored marker during the experiment, appearing indistinguishable from the black marked ant in the camera. Thus, to avoid misidentification, instead of tracking all 30 ants, we omitted the ant marked black from analysis. The excavation process was recorded for 3 hours. The ants were removed from the container and set to rest for at least 12 hours. The recorded data was analyzed to determine the 5 excavators that most contributed to tunnel construction. These active excavators were removed from the group and the experiment was repeated for an additional 3 hours. The rates of tunnel construction and the Gini coefficients were measured and compared for the first (before removal) and the second (after removal) parts of the experiment. The results were obtained in the experiments with three different colonies and averaged.

Tunnel construction rates varied little between the two phases of the experiment. In fact, the individual growth rate increased slightly: 0.58 ± 0.2 mm/ant within the first part of the experiment versus 0.67±0.3 mm/ant in the second part. The workload distribution also did not change and the Gini coefficient was 0.73±0.15 for control (first phase of experiment) and 0.62±0.06 for active removal (second phase), see Table S2. After the most active excavators from the first part were removed, several idle diggers increased their contribution to the excavation task. The contribution of the most active excavators within the first and the second parts of the experiment was comparable: 74±21% versus 74±5% of all observations in the tunnel. The most active diggers of the second part of the experiment had contributed to only 10±11.4% of total observations (546±65.8) during the first part of the experiment. Thus, individual ants were able to modify their behavior in response to the changing traffic dynamics of the tunnel.

1.3 Calculation of tunnel-width normalized ant occupancy

The control experiments from the active removal experiments were used for calculating tunnel-width normalized ant occupancy, $\bar{\lambda}$ ((average number of ants in the tunnel)/(tunnel width)). Each frame in the video (15fps*(60*60*3s) = 162000 frames) was analyzed in MATLAB to identify each colored ant using image processing techniques. The number of color blobs identified in each frame was representative of the number of visiting ants in that particular frame. The tunnel width was approximated to be 2 ant body widths (BW) following results from a previous study (*20*). The occupancy was then temporally averaged over 3 minutes chunk (15fps*(60*3s) =2700 frames) at 3 different time points in the experiment. This was repeated for 3 different experiments and the average experimental ant occupancy across these experiments is projected on the fundamental traffic diagram in Fig. 3E with shaded areas representing standard deviation from 3 experiments.

1.4 X-Ray reconstruction of ant nest

A colony of *S. invicta* fire ants excavated a 3D nest in a 25 cm wide cylindrical container filled with 240-270 μm glass beads over the course of a week. The nest was then X-ray scanned (135 keV, 2.5 mA) and CT reconstructed in 3D (Fig. 1A).

2. Cellular automata model

We used a cellular automata model to elucidate the effects of collective actions on traffic during tunnel construction. In a rectangular tunnel lattice, each cell could take one of four possible states: soil, empty/excavated space, ascending excavator, and descending excavator. The initial conditions of the simulation included the number (n) of ants excavating in a group each with body length, BL, and body width, BW, as well as the width of the tunnel (W_T), the initial length of the tunnel, and the protocol of social organization of the group. At every simulation step, the ant was characterized by its 2D position (x,y), the direction of motion, whether or not they were carrying a pellet, and probability P to return back to the tunnel after pellet deposition.

The state of the cells in the model changed by a discrete time step according to a simple set of rules. At each iteration step, a CA ant located in the tunnel moved one CA cell forward or diagonally forward ("walked") with a probability p unless the destination cell was occupied. This probability affected the duration of ant clusters and was chosen from experimental observations (9). Also, when in a cluster, a descending ant had a probability to turn back and exit the tunnel without excavation ("reversal"). Due to the geometrical constraints of the CA model, the reversal behavior was an essential to prevent jamming for infinitely long times for populations $n > 2 \cdot W_T / BW$. In the absence of the reversal behavior, unresolvable clogs consisting of $n \geq 2 \cdot W_T/BW$ ants may form which span the width of the tunnel and disrupt the excavation process. Thus, reversal behavior was implemented for all CA simulations regardless of workload distribution.

When the ant reached the tip of the tunnel, it spent several time steps excavating. The excavated pellet was transported to the entrance of the tunnel and expelled from the tunnel ("pellet deposition"). After a predefined number of pellets were collected the tunnel grew in length by 1 cell. After pellet deposition, the ant would return to the tunnel with probability P or switch to resting mode. During the pellet deposition or resting mode, the ant was neither contributing to the excavation, able to cause clogs, nor increasing tunnel density. The exit from the resting mode was also defined by probability P.

The unequal workload distribution was achieved by introducing the probability, P, to return to excavate in the tunnel after a pellet deposition. To simulate fully active ants, workers attempted to reenter the tunnel immediately after pellet deposition ($P = 1$). In groups with unequal workload distributions, the probability of the ant to return to try and return to the tunnel was unique, fixed and derived from the experimental ant workload distribution measurements as $P(\frac{n_i}{n}) = f\left(\frac{n_i}{n}\right) - f(\frac{n_i-1}{n})$, where n_i was the number of ants in a sequence from the least to the most active; n was the excavating group size, and f was a Lorenz function.

All parameters describing ant behaviors were found via experimental observation; the only parameter varied to allow the system to match experiment was the excavations to grow tunnel size by 1 cell. The rates were calculated from the slope of the tangential lines fitting the initial portion of the tunnel growth curve. The tunnel excavation rates in simulations differed greatly depending on excavation scenario. In general, the groups of active diggers ($P = 1$) were most efficient when the number of excavators in the group was small. The increase in the number of active excavators led to the formation of ant clusters, which eventually slowed the nest construction down. The unequal workload distribution $P(\frac{n_i}{n})$ in large groups of excavators allowed for reduction of ants density in the tunnel throughout the experiment and, thus, produced high nest construction rates even when the number of diggers in the excavating group was large. In large groups of diggers with unequal workload distributions, the excavation rates were insensitive to the addition of excavators.

2.1 Occupancy and flow in CA model

The CA simulations were carried out for ant groups of different sizes. The width-normalized ant occupancy and the flux were measured in L_T = 5 cell long tunnel (~2.5 cm actual length). The flux and occupancy were measured at $i = \text{floor}\left(\frac{L_T}{2}\right) + 1$ position in the simulated tunnel (Fig. S4). We calculate ant occupancy as the time-averaged number of ants in the tunnel divided by the tunnel width, W_T, in ant body widths, BW:

$$\bar{\lambda} = \frac{1}{T}\sum_{t=1}^{T} n_i(t)\, / W_T \tag{1}$$

where $n_i(t) = 1$ if the site is occupied at time t and 0 otherwise. Occupancy at a fixed site i was averaged over a time period T=3 hours. The average bi-directional flux $\bar{q}^T$ between site i and neighboring sites $i+1$ and $i-1$ was defined as

$$\bar{q} = \frac{1}{T}\sum_{t=1}^{T}\left[n_{i,i+1}(t) + n_{i,i-1}(t)\right] / W_T \tag{2}$$

where $n_{i,i+1}(t) = 1$, if the ant moved between sites i and $i+1$, and $n_{i,i-1}(t) = 1$ if the motion occurred between i and $i-1$, and zero if the motion was not detected. The flux was averaged over time T corresponding to 3 hours of experiment. The flux was normalized by the tunnel width.

We introduced these definitions to compare traffic in groups of different sizes governed both equal and unequal workload distributions. The fundamental flow diagrams (tunnel flow $\bar{q}$ vs occupancy, $\bar{\lambda}$) for each experimental condition are provided in the main text.

2.2 Clustering characterization in CA model

The implementation of unequal workload distribution reduces the immediate density of the ants in the tunnel in simulations. As a result, the number of clusters (I_c), their spatial extension (a_n) and time duration (T_c), as well as the number of ants involved in the jams C decrease, allowing for stable traffic formation (Fig. S5).

To analyze traffic, the jam was defined as agglomerations of 2 or more ants located in the neighboring cells at a simulation step k. The number of clusters was defined as the total number of agglomerations observed over 50,000 simulation steps. Each simulation step was considered independently. The site occupancy time T_c was defined as the time it takes for a particular cell occupied by an ant involved in a jam to change its value from “occupied” to “vacant”. The average spatial extension of the jam was defined as the number of cells occupied by the ants sequentially along the tunnel length. The number of ants involved in a cluster, the cite occupancy time and the spatial extension of a jam were averaged over all simulation steps and results are reported on Fig. S5.

2.2.1 Cluster Size and Frequency Dynamics in CA model

We characterized how cluster severity was affected by reversals and unequal workload distributions through an analysis of cluster formation. Clusters in 30-ant simulations were identified at each simulation time point and categorized by the number of CA ants that comprised the cluster. Any group of ants that blocked the entire tunnel width was considered a cluster. We found a prevalence of large clusters for extremely low reversal probabilities in both equal (*Fig. S26 A*) and unequal (*Fig. S26 B*) workload distributions. A minimal increase in reversal probability reduced the prevalence of the largest clusters from forming. However, even accounting for higher reversal probabilities, equal workload distributions resulted in wider distribution of cluster sizes, whereas the optimized workload distribution produced a sharper concentration of small clusters, which were more easily dispersed. Thus, cluster mitigation is most effective using both reversals and unequal work probabilities in combination.

2.3 Optimal distributions CA using a genetic algorithm

A genetic algorithm (GA) was used to search for entrance probability distributions that produced optimal digging rates. The GA is a biologically inspired optimization technique used typically to find solutions where the parameter space is large. GAs modify or evolve populations of solutions at each generation, through processes known as reproduction and mutation, towards the optimal solution. Each probability distribution for a single simulation is known as a "chromosome", and each probability for a single ant are called "genes". The set of all chromosomes at each generation is called a population. The reproduction phase requires each chromosome to be run, and depending on the on the output of the objective function, the metric by which each chromosome is measured, certain chromosomes are selected to be parents for the next generation. Our implementation used the digging rate as the objective function. The best performing chromosomes, known as the elite percent go unchanged to the next generation. The rest of the chromosomes are paired up, and a percentage, known as crossover percentage, are crossed over. Crossover is where a random site is chosen along the length of a chromosome and the genes of the paired chromosomes are switched around that point. After crossover, all genes belonging to the non-elite group of chromosomes have a chance, known as mutation probability, to be assigned a new random value. This helps to mitigate chances of becoming stuck in local minima (or maxima) of the optimized quantity.

We used MATLAB's genetic algorithm toolbox (*36*). Our selection type was the default used in MATLAB's GA toolbox, stochastic uniform. The specific values for our reproduction and mutation rates were as follows: 5% for the elite selection, 0% for the crossover fraction, and a variable number of gene was subjected to mutation according to an adaptable mutation rate, the default option for MATLAB. We used a population size of 200 probability distributions per generation, and ran 50 generations.

2.4 One at a Time (OAT) Model

2.4.1 Introduction

We model a tunnel as a one-dimensional lattice of Z sites; an ant occupies one lattice site. The tunnel has an open boundary at the left (site 0) where ants can enter and exit, and a closed boundary at the right (site N) that represents the end of the tunnel. Note that for simplicity we keep N fixed: in this model, the tunnel does not change length in time.

Each ant can move toward to the next site at rate v. Ants enter the tunnel at rate αv, which may be the same for each ant or variable. Once an ant enters the tunnel it moves to the right at rate v, but can reverse and move to the left. If an ant is blocked by another ant in front of it, it cannot move. Ants reverse at rate S either when they reach the end of the tunnel, or when they are adjacent to another ant going the opposite direction. At site 0 in the tunnel, ants moving to the left exit with rate βv.

Once an ant reaches the end of the tunnel (site Z), reverses, goes back, and exits the tunnel, it completes one cycle of digging. Since the model only allows one ant to occupy a given site (ants sterically exclude each other), the ant that completes a digging cycle is the first ant to enter the tunnel when it is empty. The ants that follow only hinder the digging process. We call this the *One-at-a-Time (OAT) model* (Fig. S13).

We define excavation rate in this model as the number of completed digging cycles over a certain time. We used kinetic Monte Carlo (kMC) simulation (see section 2.4.4 for details) methods developed in our previous work (*25*) to do simulations of this model. In simulations, we measure the total number of ants, and count events in which the tunnel has no ants in it. Model parameters that produce higher excavation rate lead to more events during which the tunnel is empty (Fig. S14).

If the inward flux leads to a time between ants entering the tunnel that is longer than the time for an ant that has already entered to reach the end of the tunnel and exit, then increasing α increases the excavation rate. However, if the time between ants entering is shorter than the digging time, most ants that enter the tunnel create traffic jams that block the digging ant from retreating. This decreases the excavation rate. Simulating the OAT model at different values of α (whereby all ants in a simulation are given an identical α) results in an intermediate peak in excavation rate as a function of α (Fig. S15). Giving all excavators an identical α is akin to the equal workload distribution in Active ants of the CA model, whereby varying α modulates the overall level of activity of all ants.

We analytically derive the excavation rate by estimating the typical time of one digging cycle. The time to complete one cycle is the sum of (a) the time for the first ant to enter the tunnel, (b) the time it takes for the digging ant to walk to the end of the tunnel and back to the entrance, and (c) the time required for all ants in the tunnel to reverse their direction. The typical time to wait for the first ant to enter the tunnel is $1/_{\alpha v}$, the inverse of the entry rate. The typical time for an ant to walk to the end of the tunnel and back is $2L_T/_v$, where L_T is the length of the tunnel. The additional time due to waiting for ants to reverse direction we estimate by noting that the typical reversal time is $1/_S$. If the tunnel were infinitely long, then the typical distance between two ants in the tunnel would be the typical time between ants entering the tunnel times the typical speed of an ant, which is $1/_{\alpha v} \times v = 1/_\alpha$. However, because the tunnel is not infinite, this distance is reduced by the ants that change direction. The typical distance an ant moves during a switching event is $v/_S$. Thus, on average, the ant moving forward and the switching ant will meet when they each have traveled half of the distance between them, $1/_2\left(1/_\alpha - v/_S\right)$. This is the typical distance that an advancing ant moves before switching because it hits another ant. This must be scaled by L to account for all the ants in the tunnel, and an additional time of $1/_S$ must be added to account for the first ant to reverse at the end of the tunnel. The overall time of a digging cycle (Fig. S20) is thus:

$$T = \frac{1}{v\alpha} + \frac{2L_T}{v} + \frac{1}{S}\left(\frac{L_T}{\frac{1}{2}\left(\frac{1}{\alpha} - \frac{v}{S}\right)} + 1\right) \quad . \tag{3}$$

Note that disagreement between the theoretical curve and the kMC simulation (Fig. S15) occurs for relatively short tunnels when there are large jamming effects: in our model, we didn't consider the size of the ants and the longest distance an advancing ant could move. Note as well that our model becomes ill defined when $v/_S > 1/_\alpha$, because the term in the denominator becomes negative. This occurs for small S, which physically occurs when reversal is so slow that the excavation rate is dominated by waiting for reversals to occur. If the switching rate at the end of the tunnel has a unique rate, g, the rate at which an excavator completes an excavation, the overall time of a digging cycle becomes:

$$T = \frac{1}{v\alpha} + \frac{2L_T}{v} + \frac{1}{S}\left(\frac{L_T - \frac{1}{2}\left(\frac{1}{\alpha} - \frac{v}{g}\right)}{\frac{1}{2}\left(\frac{1}{\alpha} - \frac{v}{S}\right)} + 1\right) + \frac{1}{g}. \quad (4)$$

2.4.2 Training an unequal workload distribution

The above model assumes that every ant has the equal workload α, and demonstrates that the excavation rate actually deteriorates if ants are too diligent (large α). This suggests that system excavation rate might be sensitive to the workload distribution. We implemented a training algorithm with the following rules:

1. The total number of ants is fixed.
2. If an ant completes a digging cycle after it goes into the tunnel (in other words, it reaches the end of the tunnel), then it increases its workload, α, by a factor of q ($\alpha_{new} = q\alpha$).
3. If an ant enters the tunnel but is hindered (i.e., it reverses before reaching the end), it decreases its workload by a factor of q ($\alpha_{new} = {}^{\alpha}/_{q}$).
4. There is a maximum workload α_{max}, which is necessary to prevent super-diligent ants from taking over all the work.

In our simulation algorithm, each ant has equal probability to be selected to *attempt* to enter the tunnel, but the ith ant has its own probability α_i to decide if it "wants" to enter or not.

Using these above rules to train simulated ants in our model, we find nearly identical workload distributions (Lorenz curves), Gini coefficients (Fig. S16), and digging rate (Fig. S17), regardless of α_i for the population. The workload distribution of the trained ants is unequal; the Lorenz curves reveal that only about half of the ants are working, while the others are idle. Further, the populations reliably converge to their final workload distribution rapidly (Fig. S23). Since traffic jams in the tunnel are controlled by the total number of ants, the model predicts that (a) a larger ant population results in a more idle ants and a higher Gini coefficient (Fig. S18), and (b) the higher the maximum workload α_{max}, the higher the Gini coefficient (Fig. S19). This occurs because the overall work has a maximum, and more working ants won't increase the work. Thus, the optimal scenario in this model is for one ant to do all the work by returning into the tunnel immediately once it goes out (i.e., $\alpha_{max} = \infty$).

2.4.3 Occupancy and flow in the OAT model

The time-and-spatial-average occupancy, $\bar{\lambda}$, (average occupancy) and the time-average flow, $\bar{q}$, (average flow) in the OAT model are similar to (*23*):

$$\bar{\lambda} = \frac{1}{T}\sum_{t=1}^{T} n_i(t)\Delta t \quad (5)$$

$$\bar{q} = \frac{1}{T}\sum_{t=1}^{T} n_{i,i-1}(t), \quad (6)$$

where $n_i(t)$ is 1 (or 0) if the site is occupied (or unoccupied) at time t at site i, and $n_{i,i-1}(t)$ is 1 (or 0) if the ant moved (or didn't move) between site i to $i-1$. The parameter Δt is 1 and $\sum_{t=1}^{T} \Delta t = T$. Measuring occupancy at the midpoint of the tunnel ($i = L_T/2$) yields:

$$\bar{\lambda} = 2\frac{\left(\frac{\frac{L_T}{2}}{\frac{1}{2}\left(\frac{1}{\alpha}-\frac{v}{S}\right)}+1\right)}{v}\left[\frac{1}{v\alpha}+\frac{2L_T}{v}+\frac{1}{S}\left(\frac{L_T}{\frac{1}{2}\left(\frac{1}{\alpha}-\frac{v}{S}\right)}+1\right)\right]^{-1} \text{ or} \tag{7}$$

$$\bar{\lambda} = 2\frac{\left(\frac{\frac{L_T}{2}-\frac{1}{2}\left(\frac{1}{\alpha}-\frac{v}{g}\right)}{\frac{1}{2}\left(\frac{1}{\alpha}-\frac{v}{S}\right)}+2\right)}{v}\left[\frac{1}{v\alpha}+\frac{2L_T}{v}+\frac{1}{S}\left(\frac{L_T-\frac{1}{2}\left(\frac{1}{\alpha}-\frac{v}{g}\right)}{\frac{1}{2}\left(\frac{1}{\alpha}-\frac{v}{S}\right)}+1\right)+\frac{1}{g}\right]^{-1}, \tag{8}$$

where $\left(\frac{\frac{L_T}{2}}{\frac{1}{2}\left(\frac{1}{\alpha}-\frac{v}{S}\right)}+1\right)$ is the number of ants that pass site $i = L_T/2$. The term $\frac{1}{v}$ is due to the corresponding staying time of an ant that stays in the site i (the length of an ant is the same as the length of a site). The last part of the equation is $1/T$, where T is the digging cycle. The second equality of the equation is the scenario of the unique switching rate at the end of the tunnel.

The average flow depends on the site as well. We defined it at the end of the tunnel, which is the same as the flow of the successfully working ant. The average flow is:

$$\bar{q} = \frac{1}{T} = \left[\frac{1}{v\alpha}+\frac{2L_T}{v}+\frac{1}{S}\left(\frac{L_T}{\frac{1}{2}\left(\frac{1}{\alpha}-\frac{v}{S}\right)}+1\right)\right]^{-1} \; or \tag{9}$$

$$= \left[\frac{1}{v\alpha}+\frac{2L_T}{v}+\frac{1}{S}\left(\frac{L_T-\frac{1}{2}\left(\frac{1}{\alpha}-\frac{v}{g}\right)}{\frac{1}{2}\left(\frac{1}{\alpha}-\frac{v}{S}\right)}+1\right)+\frac{1}{g}\right]^{-1}, \tag{10}$$

where the second equality of the equation is the scenario of the unique switching rate at the end of the tunnel. The numerator is 1 since there is only one successfully working ant in a digging cycle. Figures S21 and S22 show the occupancy-flow curves (fundamental diagram) when considering both a unique and identical switching rate for excavation at the end of the tunnel.

Agreement was achieved between the OAT model and the CA simulation for the fundamental diagram. However, some parameter tuning and scaling was required to account for differences between the models. Namely, in the CA model, unlike in the OAT model, not only are there multiple lanes, but CA ants are able to switch lanes to resolve clogs, whereas an ant in the OAT model must exit the tunnel. Additionally, for the flow-rate calculation, the CA model considers the flow of a successfully excavating worker twice, once on the way to excavate and again on the return to deposit. Whereas, in the OAT model, the flow of an excavating worker is considered only once. For fundamental diagram calculations, a tunnel length of 5 was used, as in the CA simulations.

2.4.4 The kinetic Monte Carlo simulation

We performed kinetic Monte Carlo (kMC) simulations of a discrete model with the time step t and the following rules at each time step for a one-dimensional lattice with Z sites:

1. Randomly choose a direction (towards the excavation site or towards the tunnel entrance) and site i.

2. If the site is occupied and the next site in both directions are empty, the ant steps forward with probability $v\Delta t$.
3. If the chosen site is occupied with an ant moving towards the excavation site and the next site over is occupied (or the chosen site is at the excavation site), the ant switches direction with probability $S\Delta t$.
4. If site 1 in the excavation direction is chosen, and it is empty, the ant occupied the site with the probability $v\alpha$.
5. If site 1 in the exiting direction is chosen and is occupied, the ant leaves with the probability $v\beta$ (we set $\beta = 1$ in the simulations).
6. Repeat steps 1-5 $2Z$ times total to sample all sites in both lanes.

The tunnel length is $Z = 20$ in the simulations (unless otherwise stated). We typically choose $\Delta t = 0.005$ such that the speed of the ants is $v\Delta t = 0.3125$ sites per kMC cycle, and $S\Delta t = 0.002175$ per kMC cycles (unless otherwise stated). We ran 6×10^8 kMC cycles per condition (unless otherwise stated). The simulation reaches the steady state typically after 10^6 kMC cycles in the training simulations. We measured the data by averaging the last 3×10^8 kMC cycles. We started the simulations with empty tunnels.

---

3. Robot Experiments

Robophysical experiments were conducted to test the performance and clustering dynamics of robots following each of three different behavioral protocols. The first strategy (Active, *Fig. S6*) assigned equal maximal attempted activity to all diggers: after soil deposition, each robot immediately returned to the tunnel to excavate. In the second protocol (Reversal, *Fig. S7*) the robots were also programmed to immediately resume excavation after deposition but reversed after some time not being able to reach the excavation site. In the third protocol (Lorenz, *Fig. S8*), we implemented an unequal probability to excavate derived from experimental ant workload inequalities.

Groups of robots operated in simulated environment that consisted of a table top testbed, featuring a quasi 2D tunnel and a pellet deposit area. The pellet deposit area was also used to accommodate inactive robots. The tunnel was partially filled with a cohesive simulated media made of loose rare-earth magnets (BYKES Technologies) contained in 3D-printed plastic shells 1.8 cm in outer diameter. The width of the tunnel allowed for simultaneous side-by-side tunnel excavation by two robots. In our previous laboratory experiments (*12*), *S. invicta* constructed ~ 1.5 body length wide tunnels

3.1 Robot design

Robots were designed to create an inexpensive yet functional robophysical system which could be used as a tool to study the effect of social protocols on collective excavation in confined spaces. The design of the robotic workers implements readily-available off-the shelf and open-source parts. A list of major components is shown in Table S4 [below, adopted from appendix B (*37*)]. Discussion of core components below provides insight into robot functionality and capabilities. A maximum of 4 robots was used in the experiments.

3.2 Microprocessors

Each robot utilized an Arduino Due microcontroller to handle sensor I/O, computations, and logic. The microcontroller software was set up to have three user programmable behavioral modes described in the paper: Active (Fig. S6), Reversal (Fig. S7), and Lorenz (Fig. S8). Each item in the flow chart has low-level control schemes responsible for obtaining sensor data, performing state estimation, and controlling the actuators. An Arduino Fio microcontroller was also used to handle data logging. Current, voltage and the state of the behavior mode was recorded and stored on a micro SD card for post processing.

3.3 Sensors

3.3.1 Navigation sensors

A low-cost camera system (Pixy CMUcam5) was used to accomplish most of the navigation. The camera located the simulated pink pheromone trail and supplied the Arduino Due with centroid coordinates and the size of the detected pheromone trail object. A lane following algorithm was used to guide the robot between the excavation and the deposit sites.

A magnetometer further improved navigation. A robot could be pushed off course in the event of a collision with another robot and lose sight of a simulated pheromone trail. The magnetometer would be used to recover correct heading. A priori knowledge of the test bed layout was exploited and thus the robot knew in which direction it needs to orient itself to get towards a current goal. The magnetometer simulated the sense of gravity in animals. A magnetometer was also used in conjunction with a gyroscope to obtain turning feedback. Robots would alter their turning strategy if no progress was measured while attempting to turn around.

3.3.2 Collision sensors

Two short range (15cm) infrared sensors were used to detect objects and obstacles directly ahead. In the event of an obstacle detection, the robot would attempt to steer around. The robot could detect physical interactions with the other robots or the environment using mechanical switches embedded beneath a segmented robotic shell. Each shell segment rested on a mechanical switch which was triggered by physical contacts within the environment. Thus, not only the contact, but also its approximate direction was sensed.

3.3.3 Environment manipulation sensors

An infrared proximity sensor was mounted near the robotic gripper. The sensor was occluded in the event of a successful collection of model media making this event distinguishably recognizable. The same sensor was also used to trigger excavation behavior.

3.3.4 Power management sensors

A bidirectional current sensor, along with a battery voltage level sensor were used to monitor power consumption. The robot relied on these sensors to determine if it needs to get to the charging station and recharge its single cell 3.7V Li-On battery.

3.4 Actuators

The robot locomotion was enabled by a differential wheeled drive system. The robot could drive with speeds up to 18cm/s. Two servo motors were used to operate a robotic arm used for manipulation of the simulated granular media. One servo motor actuated a robotic gripper while the other motor could raise or lower the pitch of the arm.

3.5 Mechanical Design

Figure S9 illustrates mechanical design. The robot's body was made with parts manufactured with a 3D printer. The design was modular, allowing easy access to and replacement of components. Most of the electronics (microcontrollers, power circuits, etc.) were safely hidden inside the robotic shell because the robots were expected to engage in many physical contacts.

3.6 Robot Tracking

The robots were tracked via an image intensity threshold routine (Fig. S10). For each experimental trial, an overhead camera recorded the tunnel area for about 30 minutes at 10 frames per second. For a given frame of video, the image was subtracted from an averaged background image. A threshold was then applied to identify pixels corresponding to the robots. Initial robot positions were manually approximated at the beginning of the video. The robot pixels were then divided into different regions using Voronoi cells generated with the initial robot position. The centroids of these regions were then used to recalculate the robot positions, which were subsequently used as approximations for the next frame.

3.7 Global Traffic Analysis

Excavation rate and energy expenditure where measured for excavation trials (3 trials of each experimental condition) of 2 to 4 robots and 3 different protocols as described in the beginning of supplemental Section 3. Each digging strategy produced distinct trends in tunnel density and energy expenditure (Fig. S12 B). The Reversal strategy exhibited peak excavation performance with two robots, and monotonically increasing density and energy cost for trials with more diggers. During Active strategy trials, robots would clog more frequently at the excavation site with edition of a fourth robot, resulting in a dramatic decrease in tunnel density and increase in energy expenditure. While dynamically allocating tasks through local feedback (*38*) or even controlling for equal workload (*39*) have proven useful in achieving robotic swarming goals such as foraging and construction, the simple Lorenz strategy was effective in lowering tunnel density and energy cost. Therefore, particularly for large populations, simply modulating the distribution of individual work effort and likelihood of giving up in the face of traffic jams are effective strategies in targeting optimal traffic densities.

3.8 Local cluster relaxation times

Tracking data was used to identify clusters of robots, defined as groups of robots whose center positions were within a robot length's proximity of each other. Robot lateral positions were represented as intensity potentials in a space-time intensity map, I (*Fig. S12 A*). Each robot was given a lateral intensity potential function (a half-cycle sine wave with one body length half-period was chosen) centered at the robot's lateral position. Clusters were identified as contiguous potentials. The local dynamics of these clusters were evaluated using a technique often used to study dynamic heterogeneities in non-biological active matter (*40*). At each time step, clusters were identified and evaluated using a correlation function derived from PIV cross-correlation techniques (*41*):

$$\boldsymbol{q(\tau)} = \frac{\sum_{x_1}^{x_2}(\boldsymbol{I(\tau,x)}-\bar{\boldsymbol{I}})(\boldsymbol{I(0,x)}-\bar{\boldsymbol{I}}_{\mathbf{0}})}{\sqrt{\sum_{x1}^{x2}(\boldsymbol{I(\tau,x)}-\bar{\boldsymbol{I}})^2\sum_{x1}^{x2}(\boldsymbol{I(0,x)}-\bar{\boldsymbol{I}}_{\mathbf{0}})^2}}. \quad (11)$$

The correlation overlap function, $Q(\tau) = \langle q(\tau)\rangle$ (where the brackets indicate a time average from time, $t = 0\ to\ \tau$, whereby t = 0 corresponds to the time step in which the cluster is identified), compares the spatial overlap of an aggregation (or cluster) at a specific time to the overlap of the aggregation's original lateral segment at a later time, τ (Fig. S12 B).

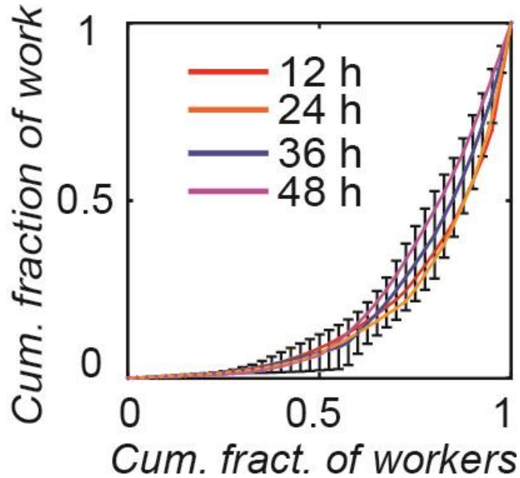

Fig. S1. Experimental Lorenz curves of ant workload distribution for individual 12-hour epochs of 48-hour trials. Error bars indicate standard deviation from multiple trials averaged over 6 trials (3 trials in ~0.25 mm diameter glass particles at W=0.1 moisture content and 3 trials in W=0.01).

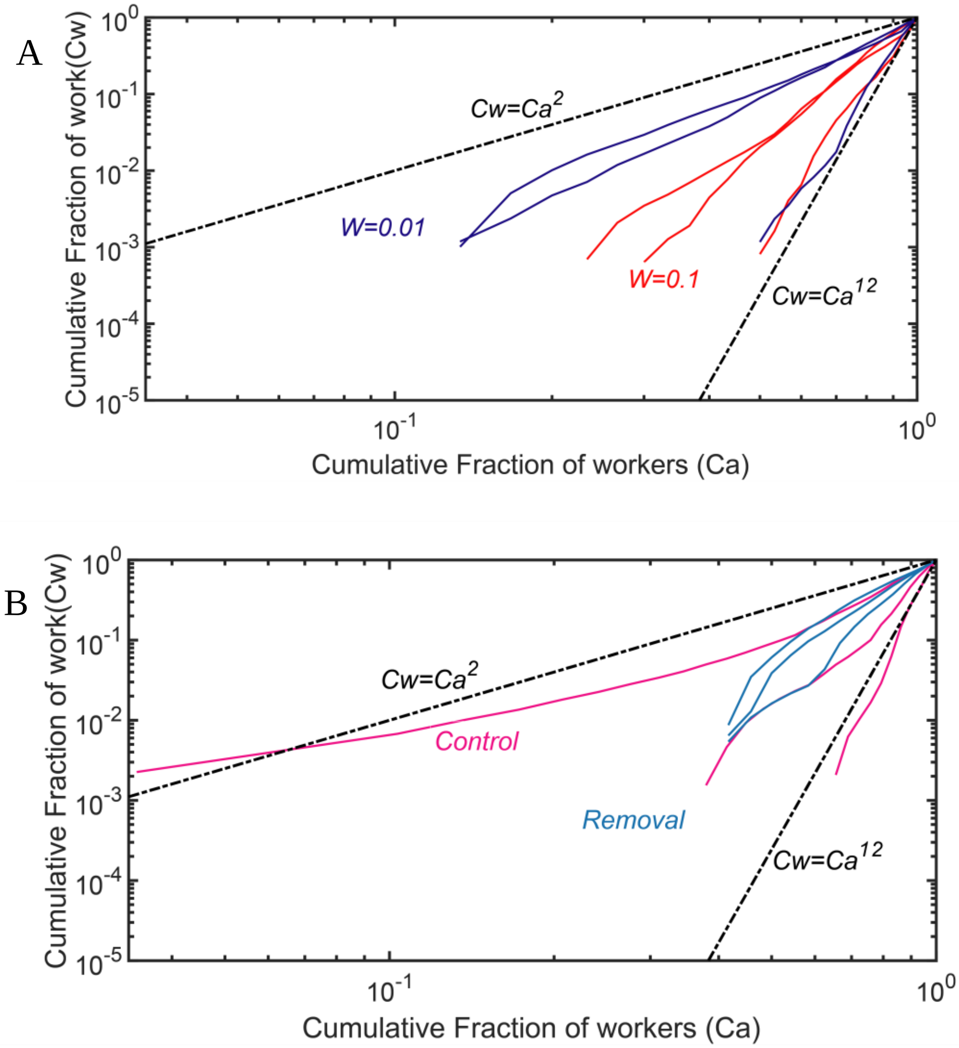

Fig. S2. Log-Log plots of Lorenz curves representing workload distributions in ant experiments (A) for different moisture contents and (B) for active removal experiment. Black dashed lines are power-law curve

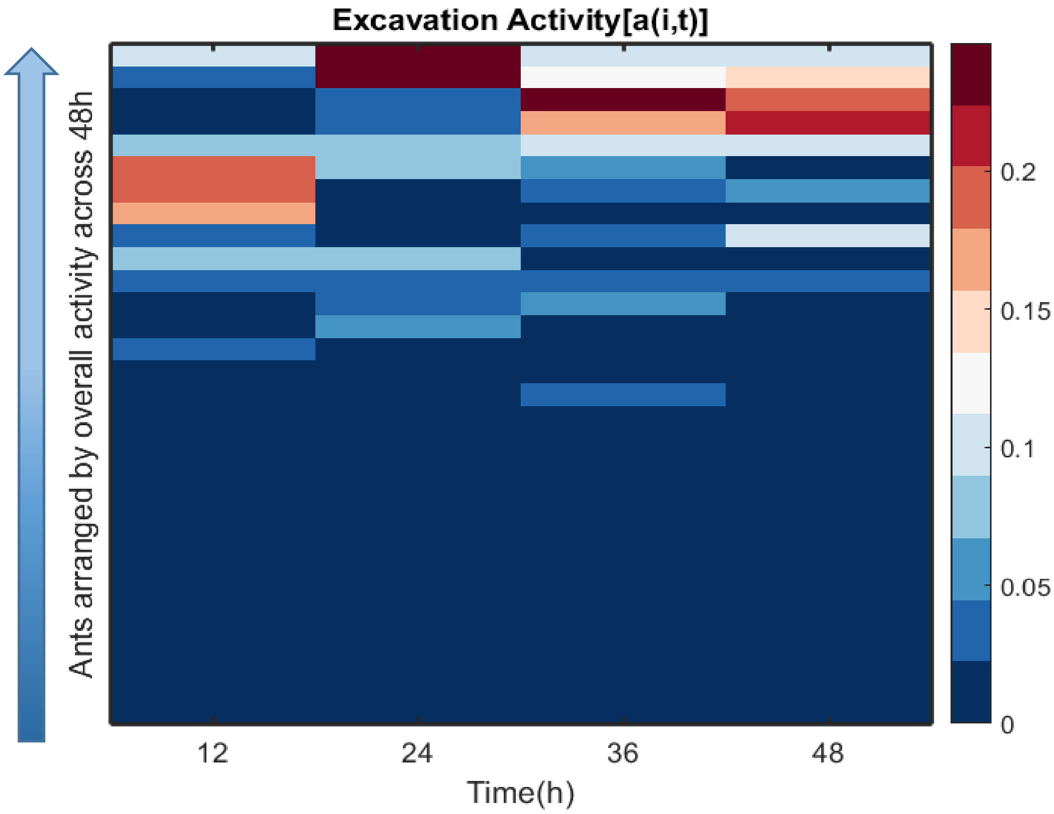

Fig. S3. Dynamic activity pattern of individual ants over different time epochs. The ants are arranged by their overall activity for 48-hours descending from bottom upwards. Excavation activity, **a(i,t)** is the number of tunnel visits per 12-hour epochs for an ant **i** divided by the total number of tunnel visits within that epoch.

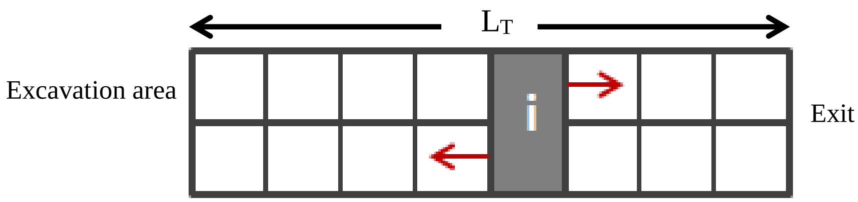

Fig. S4. Schematic of the tunnel in CA model. The occupancy of ants and the flux in the tunnel were measured at the highlighted cell i. The possible directions of ant motion are shown with red arrows.

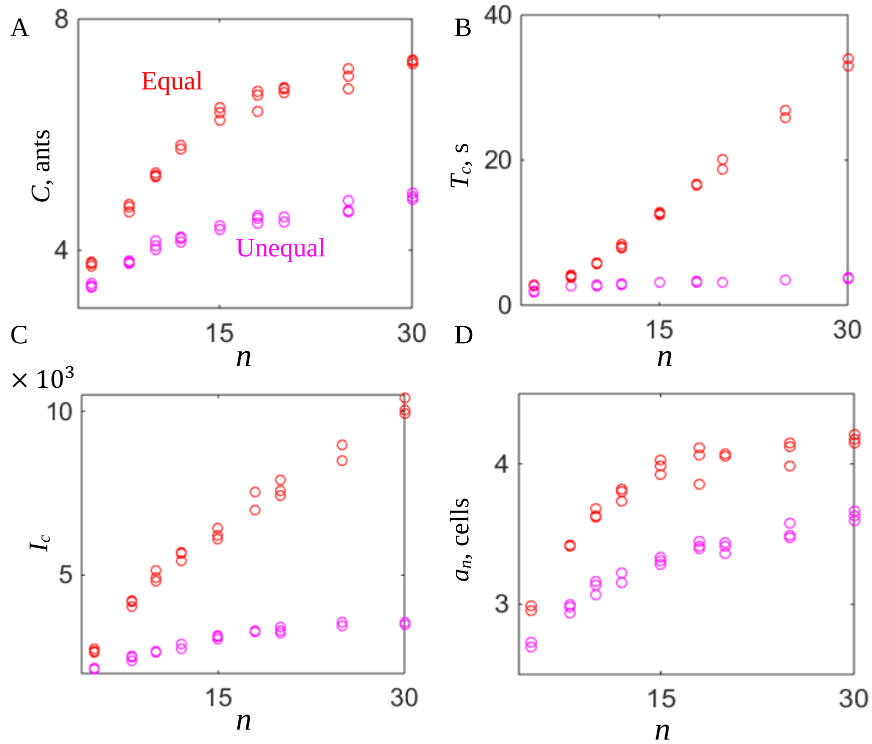

Fig. S5. Simulation results: Average number of ants involved in a jam C (A), site occupancy time T_c (B), total number of jams I_c over 50000 simulation steps (C), and average spatial extension of the jam a_n (D) plotted versus the size of the group for groups governed by equal workload distribution (red) and unequal workload distribution protocols (magenta).

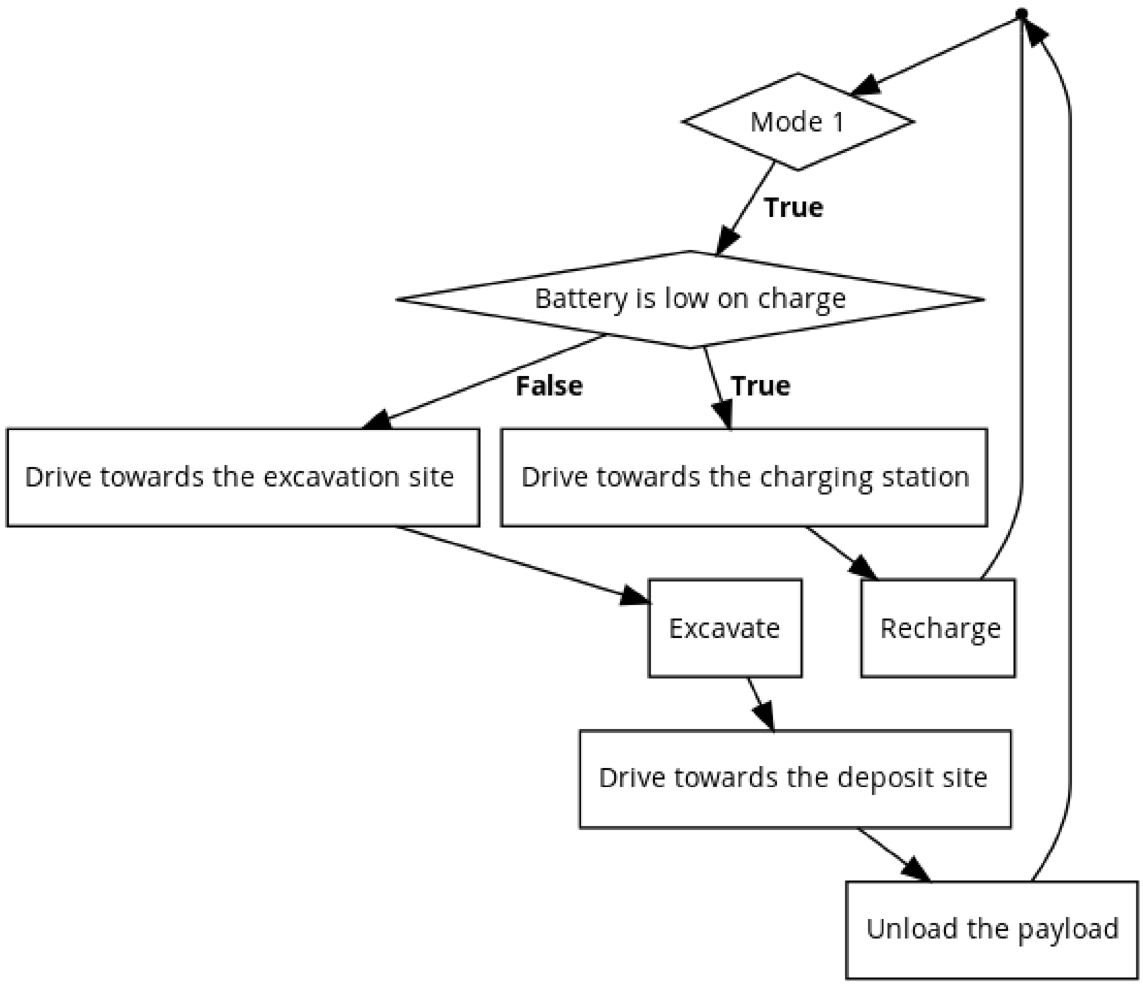

Fig. S6. Active logic flow chart.

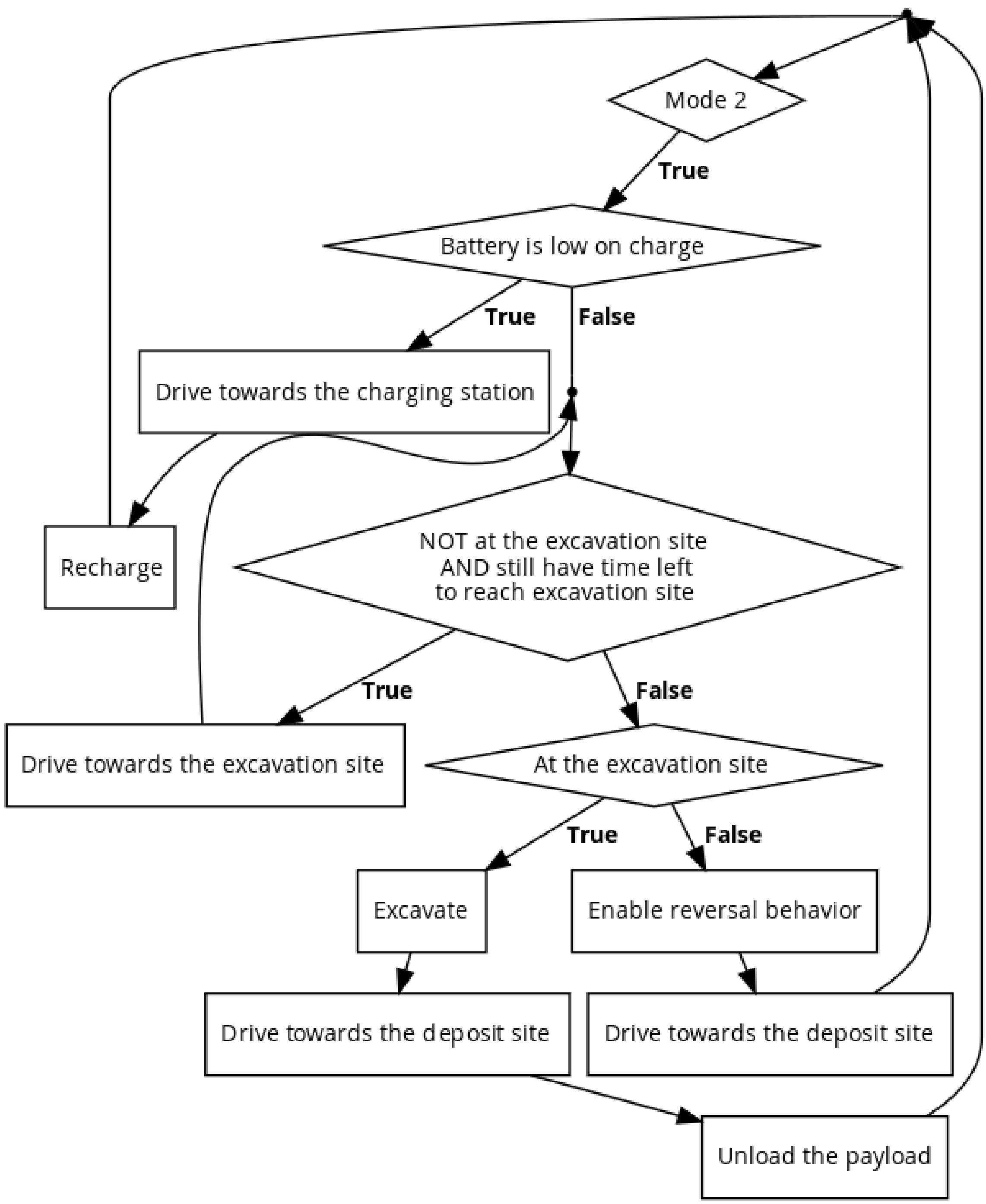

Fig. S7. Reversal logic flow chart.

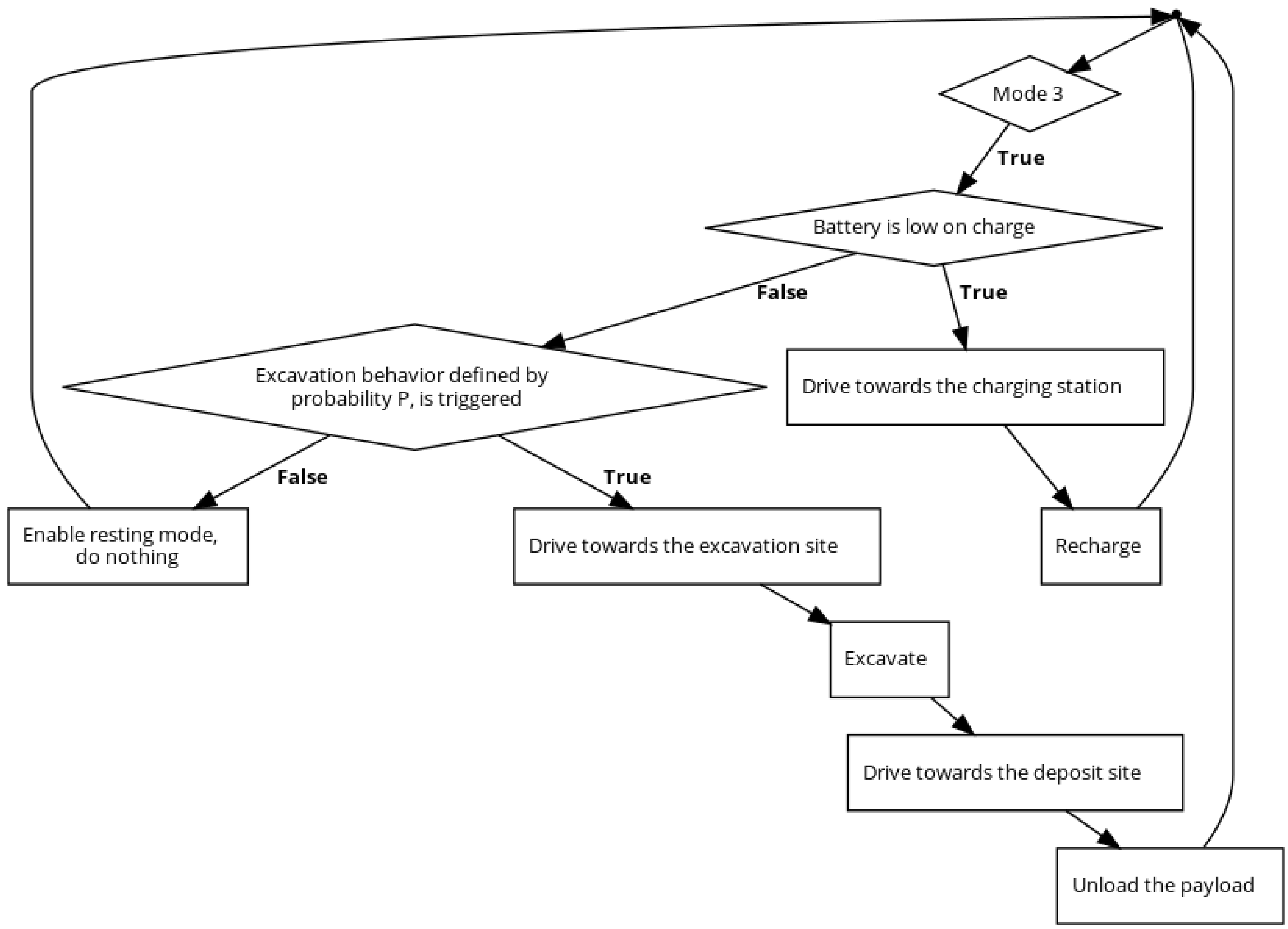

Fig. S8. Lorenz logic flow chart. Note that this logic is identical to Active if P=1. Otherwise the robot has a chance to enter resting mode outside the tunnel which last for a specified amount of time.

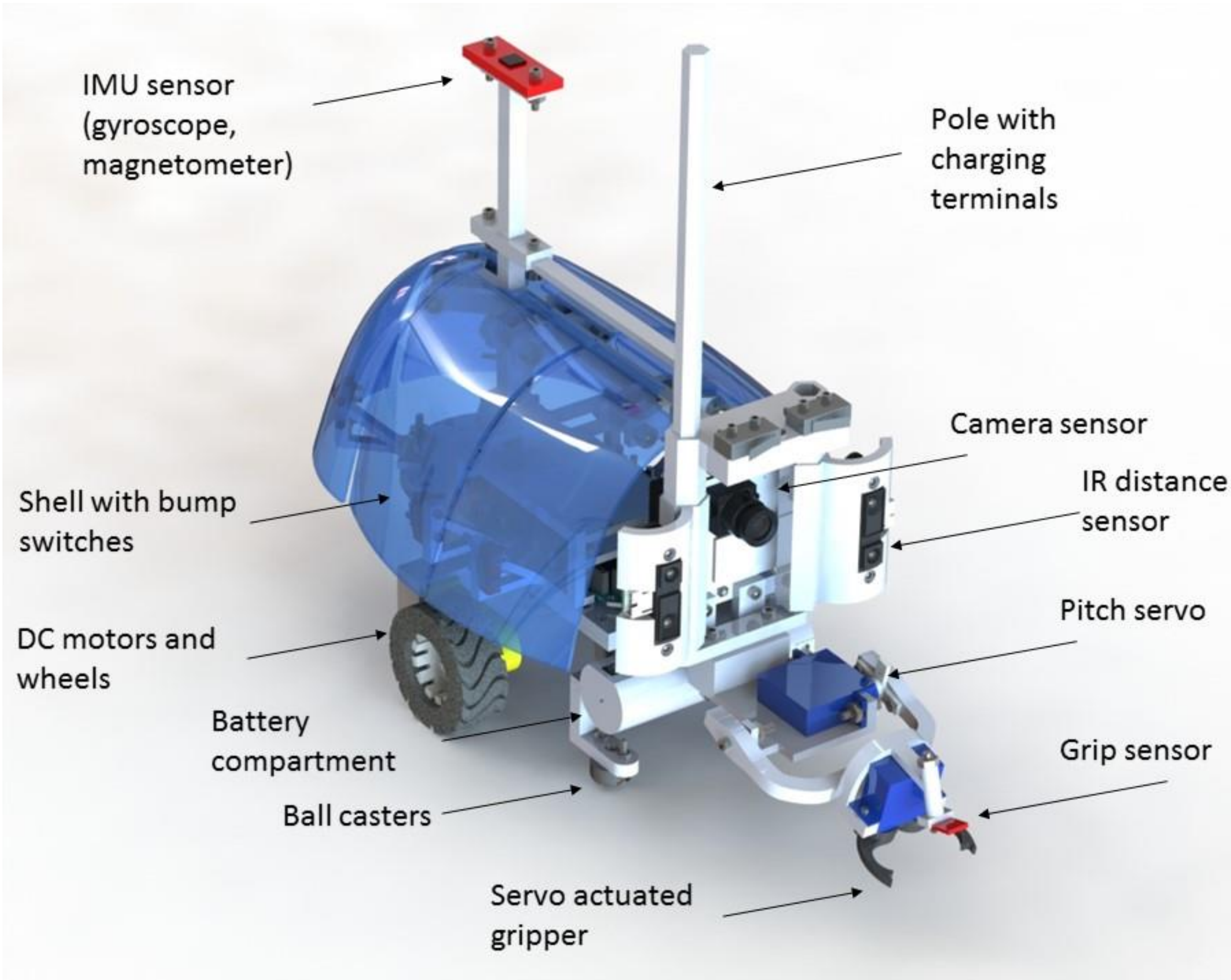

Fig. S9. Mechanical design of robots. Microcontroller and circuitry are inside the shell

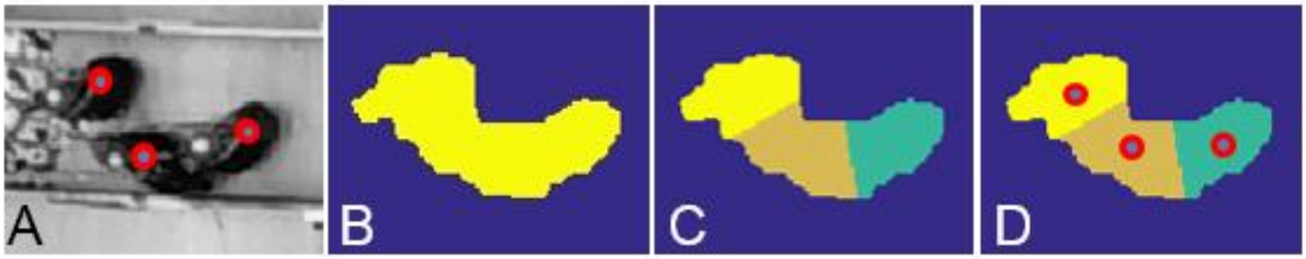

Fig. S10. Robot tracking routine. (A) Initial position estimates. (B) Threshold of background-subtracted image. (C) Voronoi divided robot regions. (D) Centroid calculated positions.

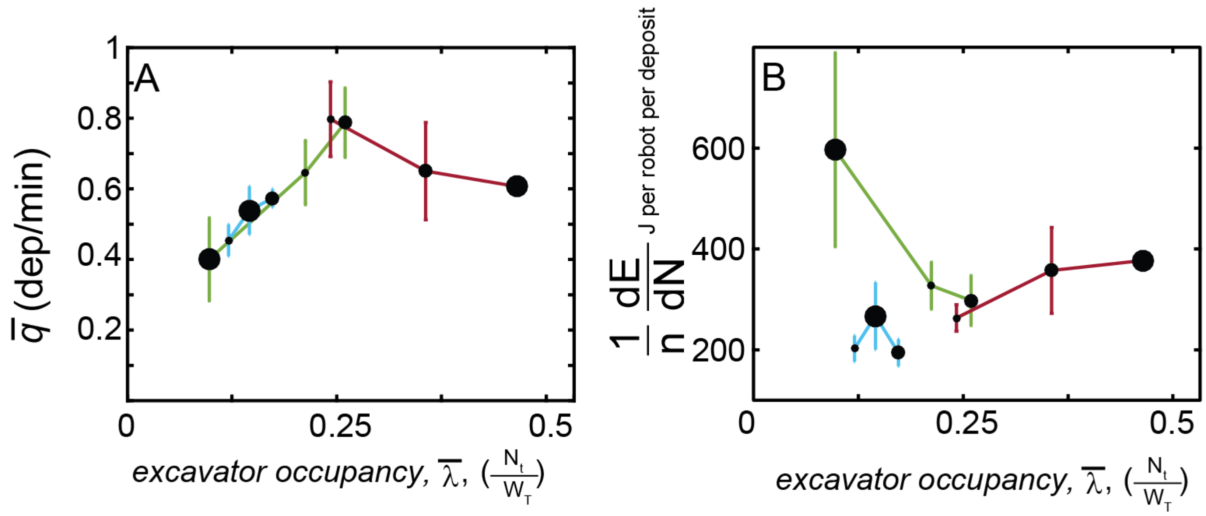

Fig. S11. Robot performance for 2 (smallest marker) to 4 (largest marker) robots using the Active (green), Reversal (maroon) or Lorenz (light blue) protocol. (A) Fundamental diagram; excavation rate, $\bar{q}$, vs excavator occupancy, $\bar{\lambda}$, where N_t is the number of robots in the tunnel area and W_T is the width of the tunnel area in robot body widths, *RW*. (B) Energy expenditure vs tunnel density.

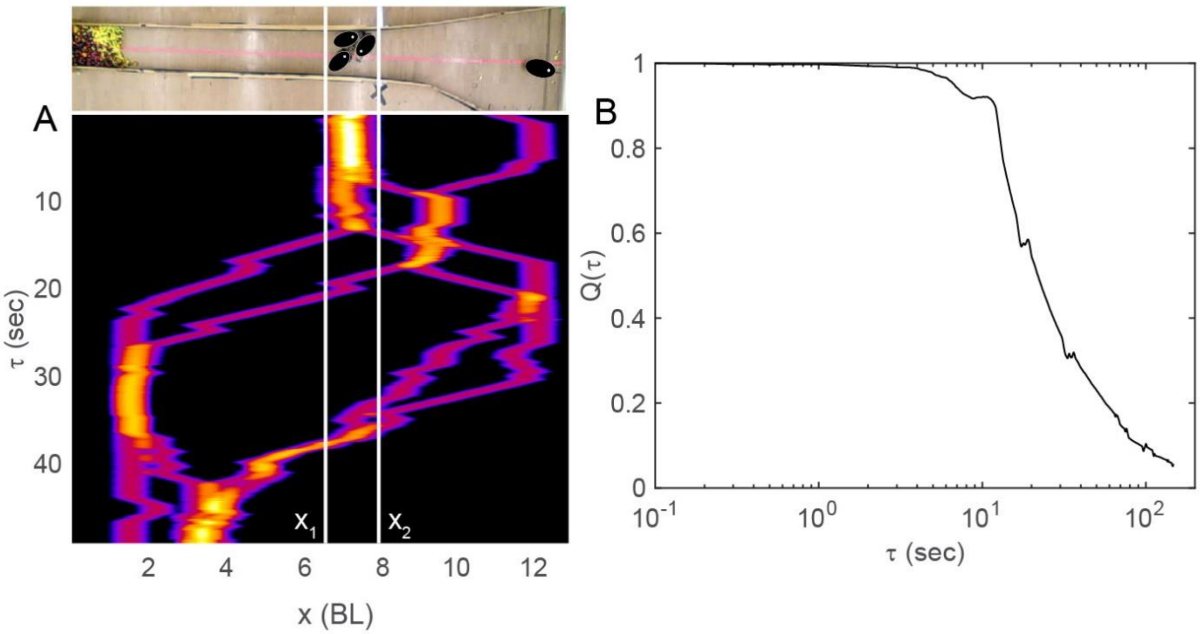

Fig. S12. Analysis of local robot clusters. (A) Sample space-time intensity map. (B) The correlation function Q(t) is calculated from the 3 robot cluster in the first frame in (A) (top panel) using image correlation algorithms used in PIV (*41*).

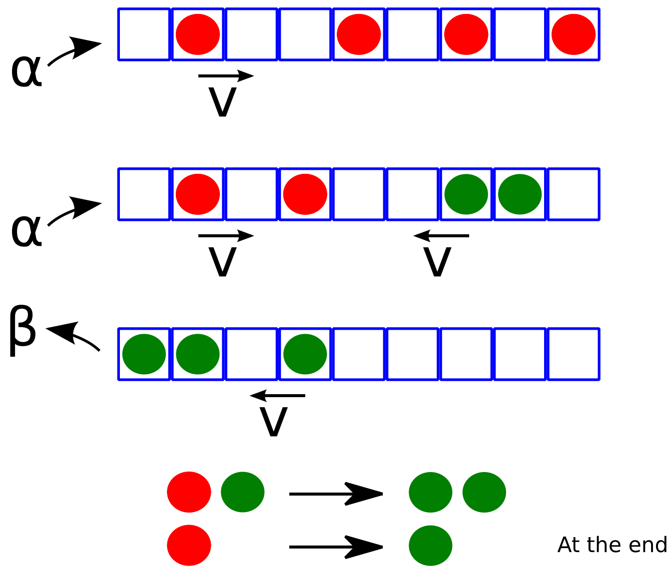

Fig. S13. Schematic of the OAT model. The red circles indicate ants moving to the right, and green moving to the left. Only one ant can occupy each site. Red ants reverse (switch to green) if they meet another green ant in front of them in the direction they move, or if they reach the end of the tunnel. The inward flux is α, which controls the average occupancy at site 0, and β is the exit rate.

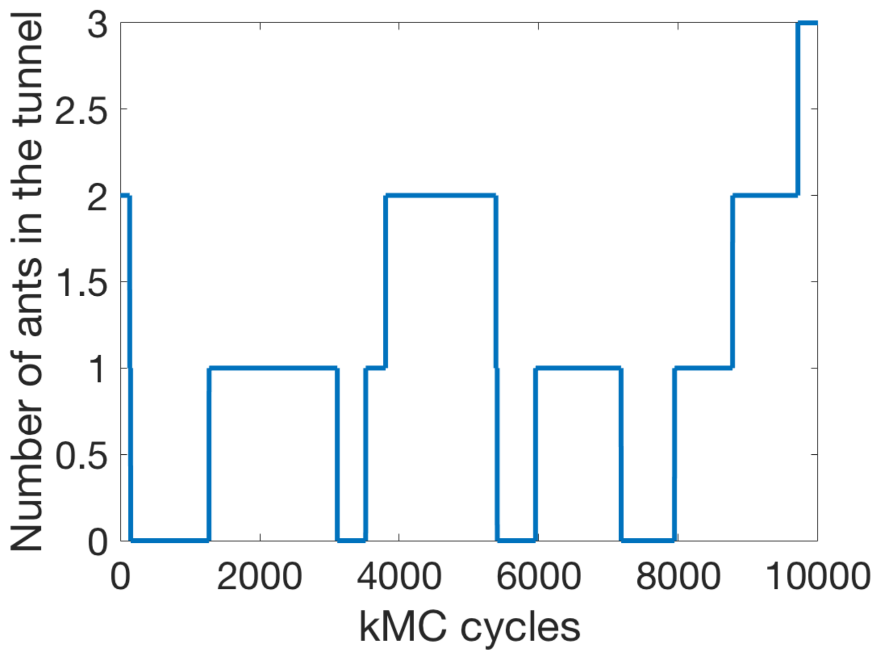

Fig. S14. Results of a simulation showing the total number of ants in the tunnel as a function of time. In this portion of the simulation, three complete digging cycles occur, because the tunnel is empty four times).

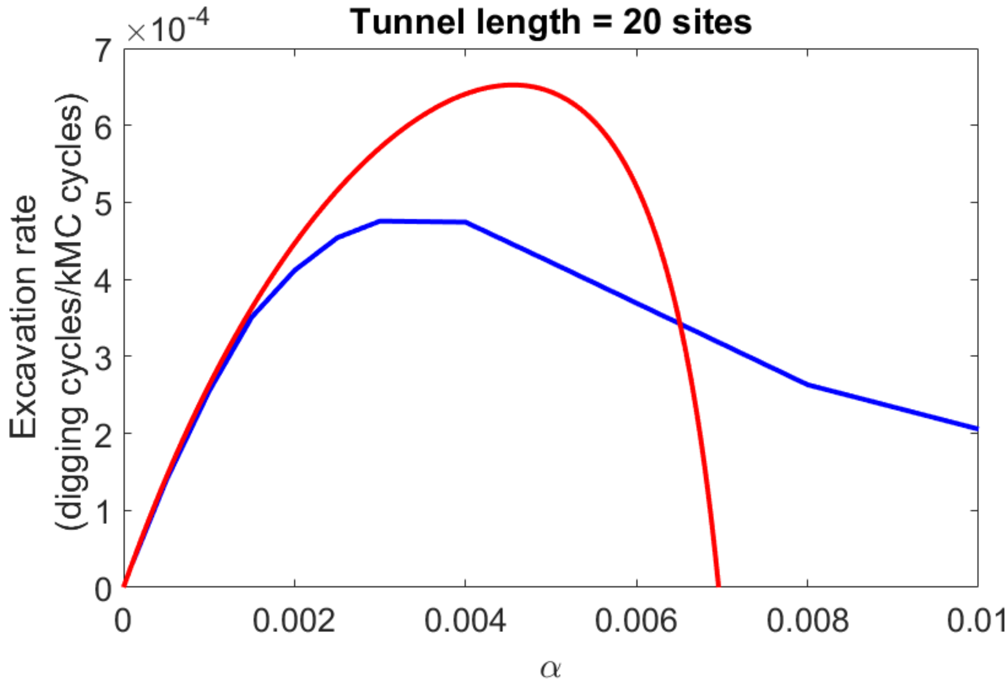

Fig. S15. Excavation rate as a function of α. Simulation results use $v = 0.3125$ sites per kMC cycles, and $S = 0.002175$ per kMC cycles. The blue curve is the simulation (kMC) results, and the red curve is the theoretical prediction ($^1/_T$, see Eq. (3)). The theory is valid if $^1/_\alpha - {}^v/_S > 0$, and the critical point in this case is $\alpha^* = 0.00456$.

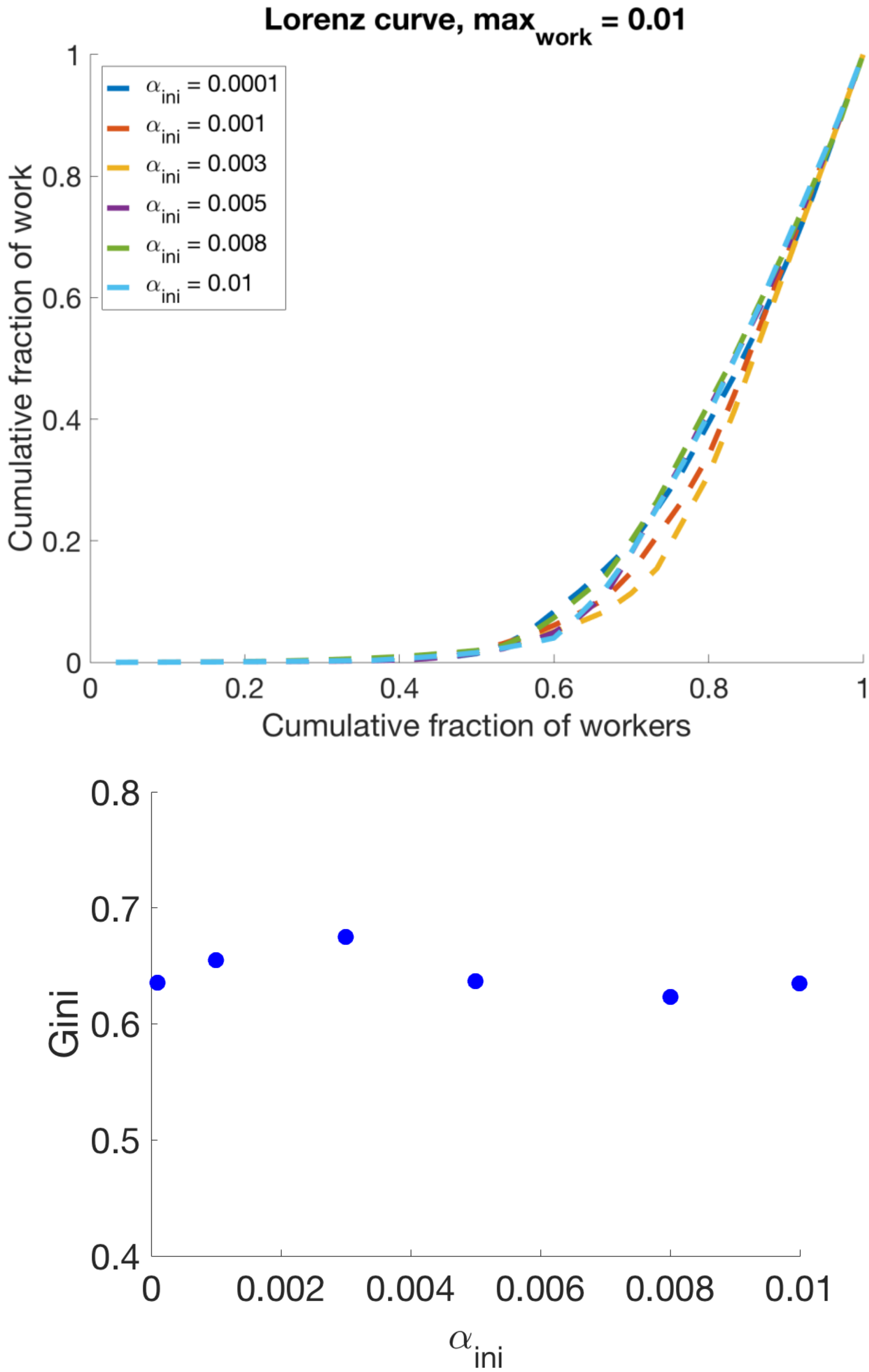

Fig. S16. The Lorenz curves and Gini coefficients that result from training with different values for the population initial workload α_{ini}. The training factor q is $1/0.9$, and the maximum workload is 0.01 (in the same units as α). The total number of ants is 30.

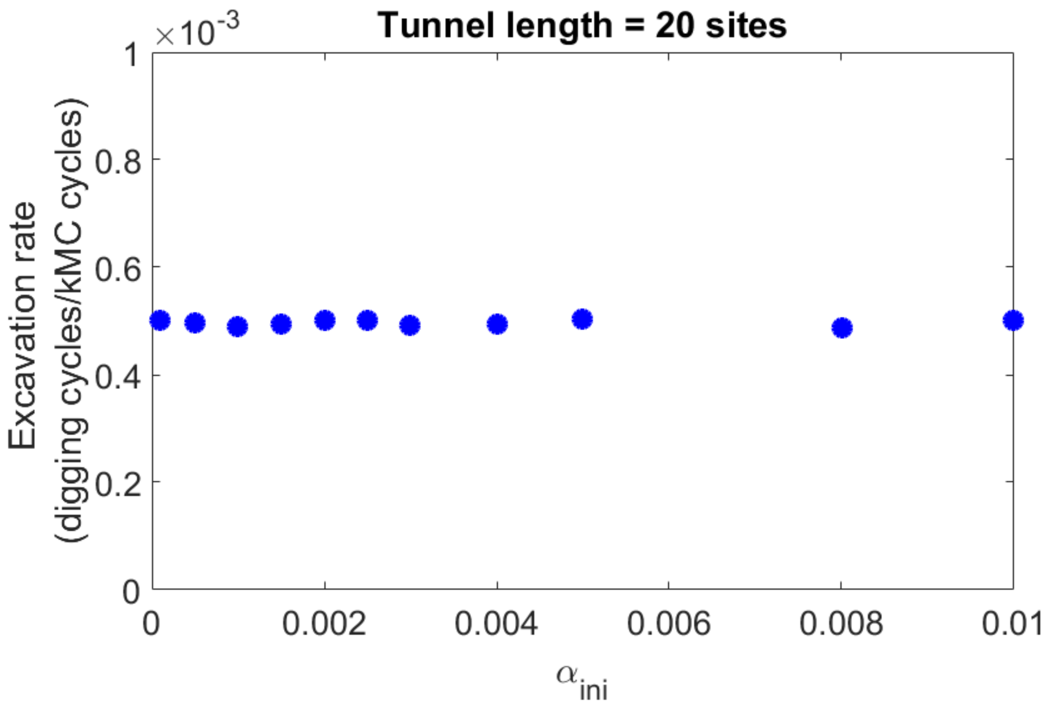

Fig. S17. Excavation rate after training. The final rate is independent of the initial population workload.

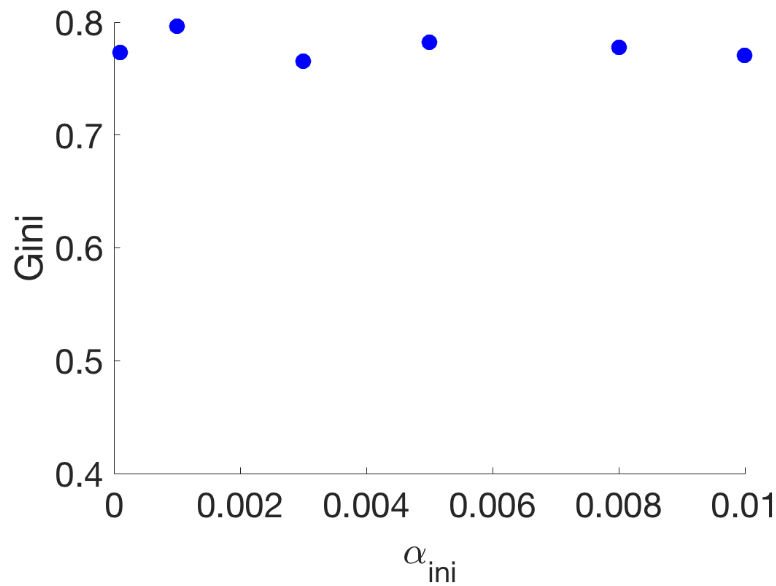

Fig. S18. The Gini coefficients with 60 ants total and $\alpha_{max} = 0.02$. The Gini coefficient is larger than that found in Fig. S18.

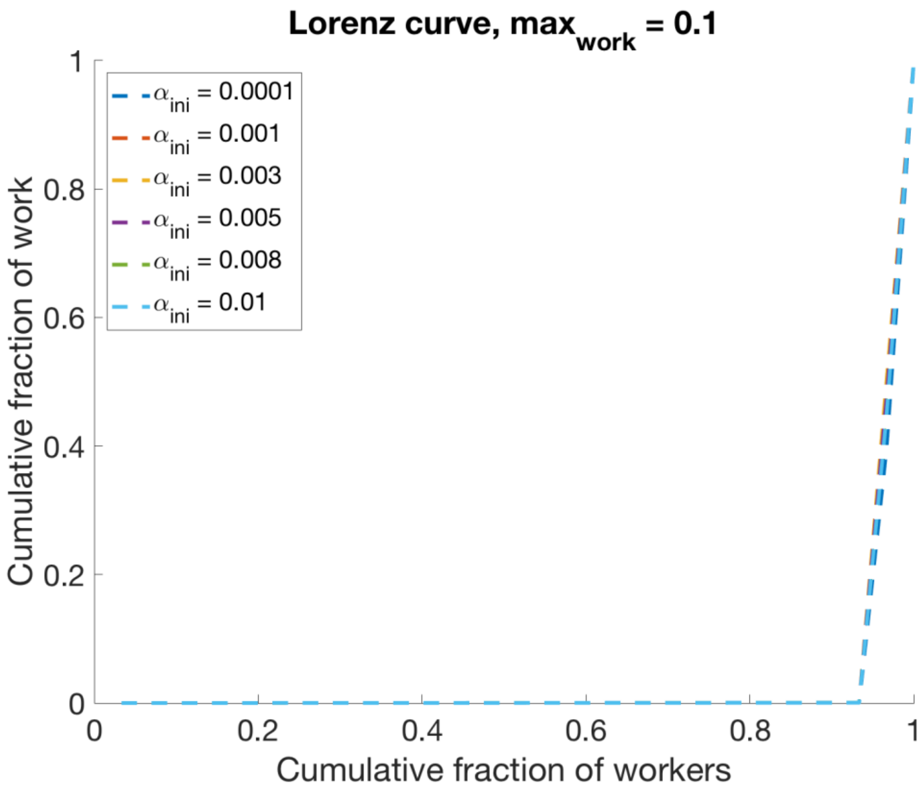

Fig. S19. Lorenz curves with different initial workload α_{ini}. The maximum workload is $\alpha_{max} = 0.1$, where their Gini coefficients are approximately 0.93.

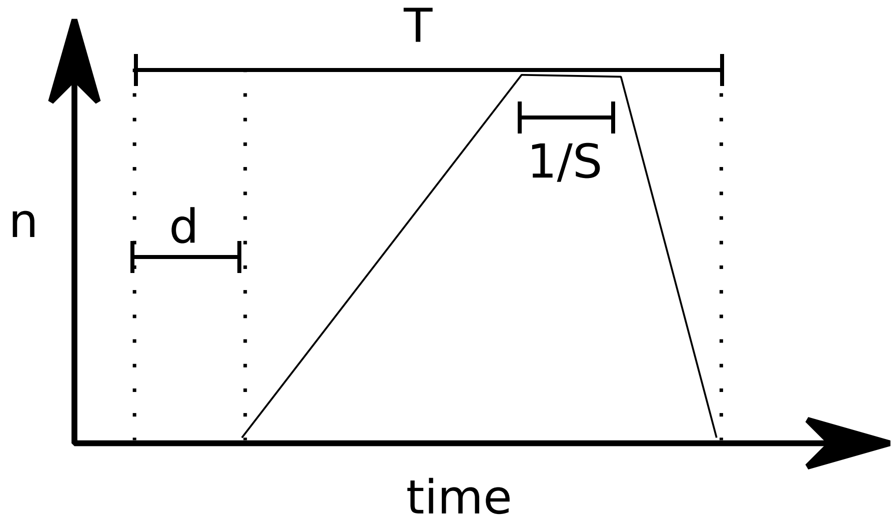

Fig. S20. Schematic of the number of ants versus time in a digging cycle. The y-axis is the overall number of ants in the tunnel, and T is the digging cycle. The delayed time d denotes the time of the first ant enter into the tunnel. The overall number of ants in the digging cycle is the area of the trapezoid, where 1=S denotes the time for the last ant to return its direction.

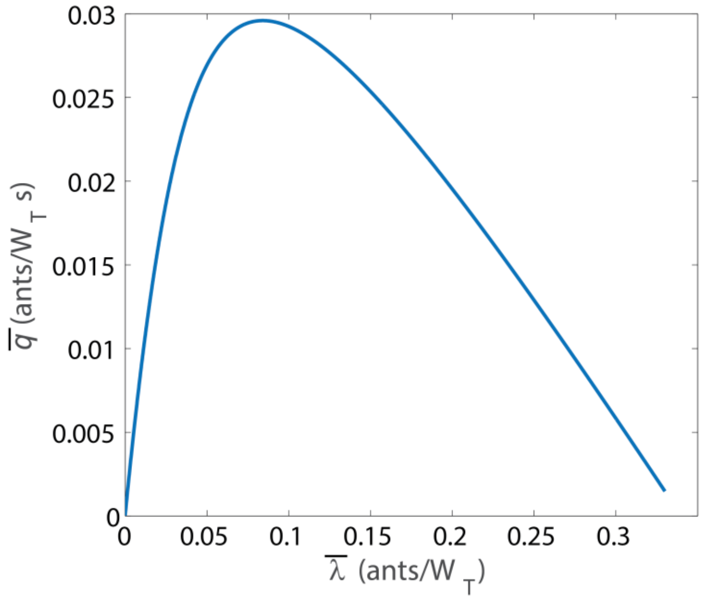

Fig. S21. Fundamental diagram: Flow rate, $\bar{q}$, vs linear density, $\bar{\lambda}$, where the switching rate at the end of the tunnel (rate of completing excavation) is identical to the rate of reversal when impeded by a retreating excavator.

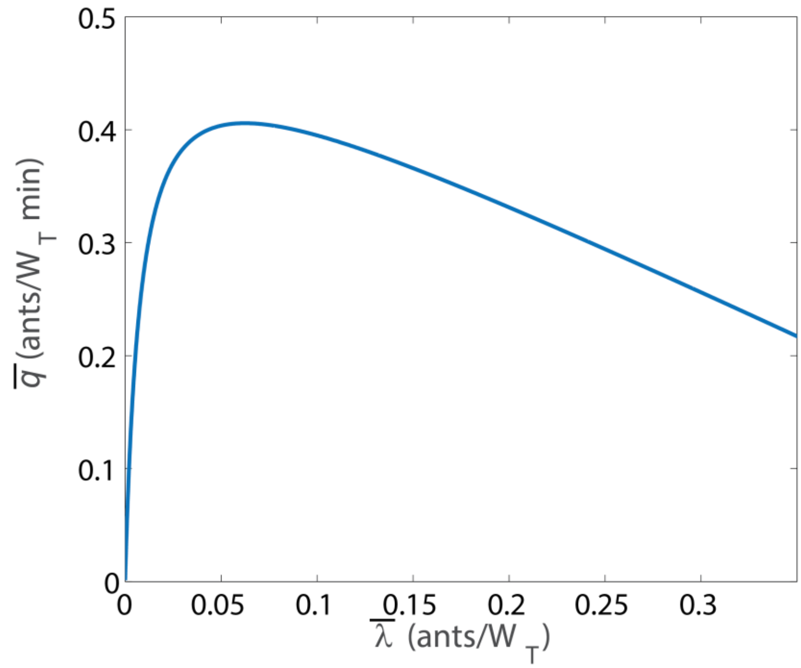

Fig. S22. Fundamental diagram: Flow rate, $\bar{q}$, vs linear density, $\bar{\lambda}$, with the unique switching rate at the end of the tunnel g = 0.005v.

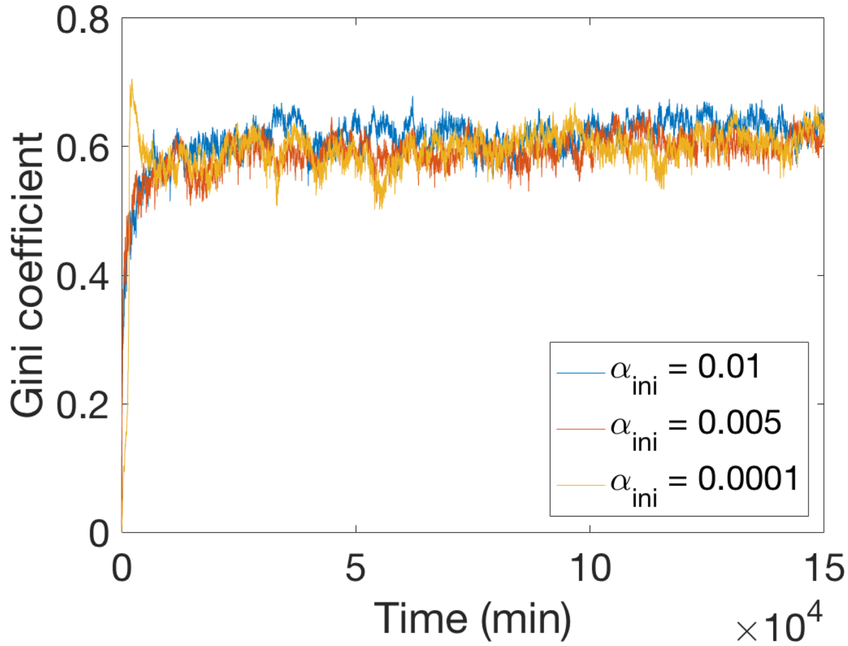

Fig. S23. Gini coefficient vs. time for different initial values of α during kMC simulation of the OAT model in which α changes over time as individual ants increase or decrease their likelihood of reentering the tunnel depending if they reversed before successfully digging.

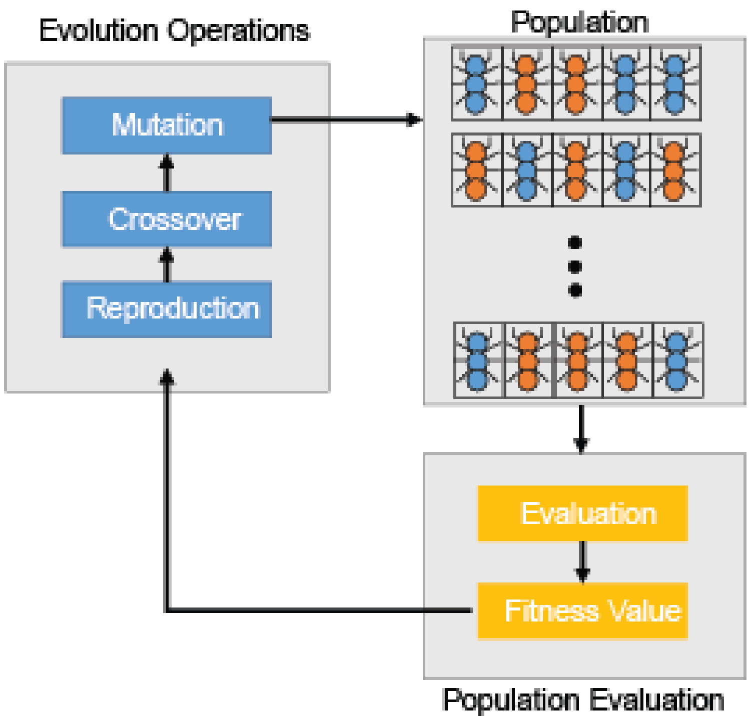

Fig. S24. Diagram illustration of genetic algorithm.

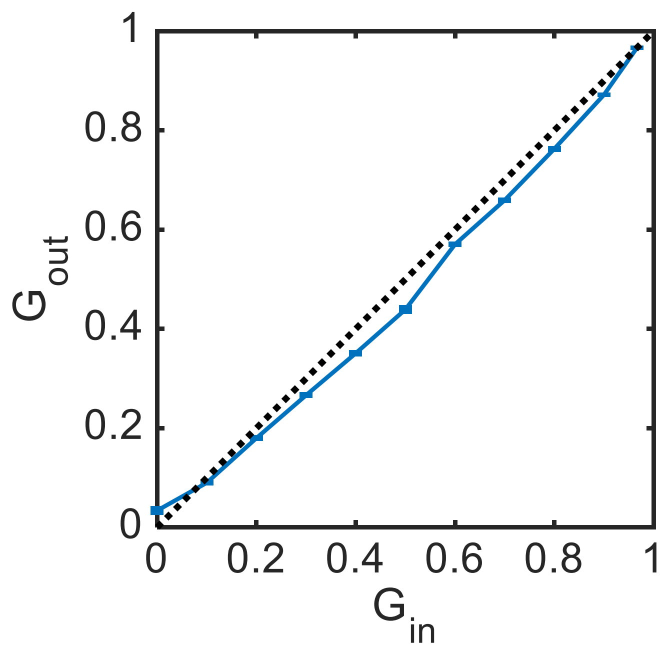

Fig. S25. Measured Gini vs. assigned Gini coefficient for system where initial tunnel length L=5 BL, with 30 ants digging for 24 hours. Each point is mean of 5 simulations with error bars shown

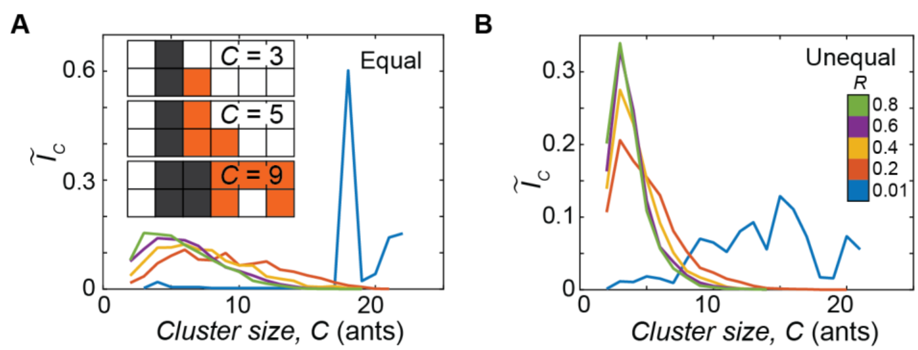

Fig. S26. Proportional number of CA ant clusters, $\tilde{I}_C = I_C/I_{total}$, of different sizes, C, measured over 24 hours for (A) equal and (B) unequal (optimized for 30 CA ants) workload distributions at different reversal probabilities (blue: 0.01, red: 0.2, yellow: 0.4, purple: 0.6, green: 0.8). Sample illustrations for different cluster sizes in (A) inset.

Table S1: Gini coefficients for primary ant digging experiment by epoch

Colony	Moisture	Gini(0-12)	Gini(12-24)	Gini(24-36)	Gini(36-48)	Total 48h
12	10	0.74	0.75	0.76	0.78	0.67
12	1	0.53	0.71	0.77	0.70	0.58
16	10	0.80	0.79	0.80	0.67	0.71
16	1	0.85	0.82	0.83	0.87	0.81
3	10	0.77	0.87	0.90	0.91	0.82
3	1	0.62	0.79	0.70	0.67	0.56

Table S2: Gini Coefficients for ant removal experiments

Colony	Moisture	Removal	Gini
1	10	before	0.85
1	10	after	0.57
2	10	before	0.76
2	10	after	0.69
3	10	before	0.56
3	10	after	0.62

Table S3: Parameters for CA Simulation

Time step, Dt	0.5 s
Ant size	1 cell
Tunnel width (w)	2
Reversal probability (R)	0.34
Sim length	172800 steps (24 hrs)
Time to drop pellet	20 steps
Probability to move sideways (p)	0.52
Probability to move forwards	1
Excavations to grow tunnel size by 1 cell	200
Rest Time	600 steps

Table S4: Robotic ant components

Core components	**Purpose**
Pixy Camera	Navigation
Magnetometer	Navigation
Gyroscope	Navigation
DC gearmotors	Locomotion
IR Distance Sensors	Obstacle avoidance
Contact Switches	Collision detection
Servo Motors	Environment manipulation
Proximity Sensor	Simulated media feedback
Li-On Battery, Single cell	Power source
Voltage Sensor	Power management

Current Sensor	Power management
Arduino FIO	Data logging
Arduino DUE	Sensor I/O, robot control

Supplemental Movie Captions

Movie S1
Ant activity experiments: Video of an ant (yellow-orange) giving up/reversing when faced with heavy traffic in tunnel.

Movie S2
Ant simulation**:** Animation of a Cellular Automata (CA) simulation of ants with Active protocol (equal workload distribution) vs. Lorenz protocol (unequal workload). Cell colors denote soil (light grey), tunnel (white). CA ants moving towards the excavation site (orange) and exiting the tunnel (dark grey).

Movie S3
Single robot excavation: Video of a robophysical excavator following a pink line (a guidance trail) and excavating model cohesive granular media; the plastic hollow shells are filled with loose magnets enabling clumps to form.

Movie S4
Collective clogging in robot excavation: Video of robophysical excavators encountering and resolving a clog while excavating model cohesive granular media.

Movie S5
Robophysical experiments comparing excavation protocols**:** Video comparing Active (top), Reversal (middle) and Lorenz (bottom) protocols implemented on excavating robots. Each Active robot exhibited maximum levels of activity. Reversal robots had a small probability to abandon the excavation attempt if the excavation area could not be reached within pre-defined time interval. Each Lorenz robot was assigned a distinct probability to re-enter tunnel after excavation. The proportion of idle and active robots is similar to observations of ant behavior.

References and Notes

1. A. Okubo, Dynamical aspects of animal grouping: Swarms, schools, flocks, and herds. *Adv. Biophys.* **22**, 1–94 (1986). doi:10.1016/0065-227X(86)90003-1 Medline

2. M. Brambilla, E. Ferrante, M. Birattari, M. Dorigo, Swarm robotics: A review from the swarm engineering perspective. *Swarm Intell.* **7**, 1–41 (2013). doi:10.1007/s11721-012-0075-2

3. M. Marchetti, J. F. Joanny, S. Ramaswamy, T. B. Liverpool, J. Prost, M. Rao, R. A. Simha, Hydrodynamics of soft active matter. *Rev. Mod. Phys.* **85**, 1143–1189 (2013). doi:10.1103/RevModPhys.85.1143

4. D. Helbing, Traffic and related self-driven many-particle systems. *Rev. Mod. Phys.* **73**, 1067–1141 (2001). doi:10.1103/RevModPhys.73.1067

5. N. C. Darnton, L. Turner, S. Rojevsky, H. C. Berg, Dynamics of bacterial swarming. *Biophys. J.* **98**, 2082–2090 (2010). doi:10.1016/j.bpj.2010.01.053 Medline

6. E. Méhes, T. Vicsek, Collective motion of cells: From experiments to models. *Integr. Biol. (Camb.)* **6**, 831–854 (2014). doi:10.1039/C4IB00115J Medline

7. A. Garcimartín, J. M. Pastor, L. M. Ferrer, J. J. Ramos, C. Martín-Gómez, I. Zuriguel, Flow and clogging of a sheep herd passing through a bottleneck. *Phys. Rev. E Stat. Nonlin. Soft Matter Phys.* **91**, 022808 (2015). doi:10.1103/PhysRevE.91.022808 Medline

8. L. Giomi, N. Hawley-Weld, L. Mahadevan, Swarming, swirling and stasis in sequestered bristle-bots. *Proc. R. Soc. London A Math. Phys. Sci.* **469**, 20120637 (2013). doi:10.1098/rspa.2012.0637

9. N. Gravish, G. Gold, A. Zangwill, M. A. D. Goodisman, D. I. Goldman, Glass-like dynamics in confined and congested ant traffic. *Soft Matter* **11**, 6552–6561 (2015). doi:10.1039/C5SM00693G Medline

10. D. M. Gordon, The organization of work in social insect colonies. *Nature* **380**, 121–124 (1996). doi:10.1038/380121a0

11. D. Cassill, W. R. Tschinkel, S. B. Vinson, Nest complexity, group size and brood rearing in the fire ant, *Solenopsis invicta*. *Insectes Soc.* **49**, 158–163 (2002). doi:10.1007/s00040-002-8296-9

12. N. Gravish, D. Monaenkova, M. A. Goodisman, D. I. Goldman, Climbing, falling, and jamming during ant locomotion in confined environments. *Proc. Natl. Acad. Sci. U.S.A.* **110**, 9746–9751 (2013). doi:10.1073/pnas.1302428110 Medline

13. D. Monaenkova, N. Gravish, G. Rodriguez, R. Kutner, M. A. D. Goodisman, D. I. Goldman, Behavioral and mechanical determinants of collective subsurface nest excavation. *J. Exp. Biol.* **218**, 1295–1305 (2015). doi:10.1242/jeb.113795 Medline

14. V. Linevich, D. Monaenkova, D. I. Goldman, Robophysical study of excavation in confined environments. *Artif. Life Robot.* **21**, 460–465 (2016). doi:10.1007/s10015-016-0317-2

15. P. Tenczar, C. C. Lutz, V. D. Rao, N. Goldenfeld, G. E. Robinson, Automated monitoring reveals extreme interindividual variation and plasticity in honeybee foraging activity levels. *Anim. Behav.* **95**, 41–48 (2014). doi:10.1016/j.anbehav.2014.06.006

16. E. J. Robinson, O. Feinerman, N. R. Franks, Flexible task allocation and the organization of work in ants. *Proc. Biol. Sci.* **276**, 4373–4380 (2009). doi:10.1098/rspb.2009.1244 Medline

17. D. M. Gordon, The evolution of the algorithms for collective behavior. *Cell Syst.* **3**, 514–520 (2016). doi:10.1016/j.cels.2016.10.013 Medline

18. V. Fourcassié, A. Dussutour, J. L. Deneubourg, Ant traffic rules. *J. Exp. Biol.* **213**, 2357–2363 (2010). doi:10.1242/jeb.031237 Medline

19. A. John, A. Schadschneider, D. Chowdhury, K. Nishinari, Collective effects in traffic on bi-directional ant trails. *J. Theor. Biol.* **231**, 279–285 (2004). doi:10.1016/j.jtbi.2004.06.022 Medline

20. N. Gravish, M. Garcia, N. Mazouchova, L. Levy, P. B. Umbanhowar, M. A. D. Goodisman, D. I. Goldman, Effects of worker size on the dynamics of fire ant tunnel construction. *J. R. Soc. Interface* **9**, 3312–3322 (2012). doi:10.1098/rsif.2012.0423 Medline

21. C. R. Reid, M. J. Lutz, S. Powell, A. B. Kao, I. D. Couzin, S. Garnier, Army ants dynamically adjust living bridges in response to a cost-benefit trade-off. *Proc. Natl. Acad. Sci. U.S.A.* **112**, 15113–15118 (2015). doi:10.1073/pnas.1512241112 Medline

22. C. Gershenson, D. Helbing, When slower is faster. *Complexity* **21**, 9–15 (2015). doi:10.1002/cplx.21736

23. K. Nagel, M. Schreckenberg, A cellular automaton model for freeway traffic. *J. Phys. I* **2**, 2221–2229 (1992). doi:10.1051/jp1:1992277

24. R. Kühne, "Traffic patterns in unstable traffic flow on freeways," in *Highway Capacity and Level of Service: Proceedings of the International Symposium on Highway Capacity, Karlsruhe, 24–27 July 1991*, U. Brannolte, Ed. (CRC Press, 1991).

25. H.-S. Kuan, M. D. Betterton, Phase-plane analysis of the totally asymmetric simple exclusion process with binding kinetics and switching between antiparallel lanes. *Phys. Rev. E* **94**, 022419 (2016). doi:10.1103/PhysRevE.94.022419 Medline

26. J. Aguilar, T. Zhang, F. Qian, M. Kingsbury, B. McInroe, N. Mazouchova, C. Li, R. Maladen, C. Gong, M. Travers, R. L. Hatton, H. Choset, P. B. Umbanhowar, D. I. Goldman, A review on locomotion robophysics: The study of movement at the intersection of robotics, soft matter and dynamical systems. *Rep. Prog. Phys.* **79**, 110001 (2016). doi:10.1088/0034-4885/79/11/110001 Medline

27. M. J. Matarić, "Designing emergent behaviors: From local interactions to collective intelligence," in *From Animals to Animats 2: Proceedings of the Second International Conference on Simulation of Adaptive Behavior*, J.-A. Meyer, H. L. Roitblat, S. W. Wilson, Eds. (MIT Press, 1993), pp. 432–441.

28. U. Borrmann, L. Wang, A. D. Ames, M. Egerstedt, Control barrier certificates for safe swarm behavior. *IFAC-PapersOnLine* **48**, 68–73 (2015). doi:10.1016/j.ifacol.2015.11.154

29. G. S. Redner, M. F. Hagan, A. Baskaran, Structure and dynamics of a phase-separating active colloidal fluid. *Phys. Rev. Lett.* **110**, 055701 (2013). doi:10.1103/PhysRevLett.110.055701 Medline

30. D. I. Goldman, H. L. Swinney, Signatures of glass formation in a fluidized bed of hard spheres. *Phys. Rev. Lett.* **96**, 145702 (2006). doi:10.1103/PhysRevLett.96.145702 Medline

31. H.-S. Kuan, R. Blackwell, L. E. Hough, M. A. Glaser, M. D. Betterton, Hysteresis, reentrance, and glassy dynamics in systems of self-propelled rods. *Phys. Rev. E Stat. Nonlin. Soft Matter Phys.* **92**, 060501 (2015). doi:10.1103/PhysRevE.92.060501 Medline

32. K. Jayaram, R. J. Full, Cockroaches traverse crevices, crawl rapidly in confined spaces, and inspire a soft, legged robot. *Proc. Natl. Acad. Sci. U.S.A.* **113**, E950–E957 (2016). doi:10.1073/pnas.1514591113 Medline

33. S. Li, Q. Jiang, S. Liu, Y. Zhang, Y. Tian, C. Song, J. Wang, Y. Zou, G. J. Anderson, J.-Y. Han, Y. Chang, Y. Liu, C. Zhang, L. Chen, G. Zhou, G. Nie, H. Yan, B. Ding, Y. Zhao, A DNA nanorobot functions as a cancer therapeutic in response to a molecular trigger in vivo. *Nat. Biotechnol.* **36**, 258–264 (2018). doi:10.1038/nbt.4071 Medline

34. W. Liu, A. F. Winfield, J. Sa, J. Chen, L. Dou, Towards energy optimization: Emergent task allocation in a swarm of foraging robots. *Adapt. Behav.* **15**, 289–305 (2007). doi:10.1177/1059712307082088

35. D. Jouvenaz, G. Allen, W. Banks, D. P. Wojcik, A survey for pathogens of fire ants, *Solenopsis* spp., in the southeastern United States. *Fla. Entomol.* **60**, 275–279 (1977). doi:10.2307/3493922

36. MathWorks, Global Optimization Toolbox (R2016a) (2016).

37. V. Linevich, Master's thesis, Georgia Institute of Technology, (2015).

38. M. J. Krieger, J.-B. Billeter, The call of duty: Self-organised task allocation in a population of up to twelve mobile robots. *Robot. Auton. Syst.* **30**, 65–84 (2000). doi:10.1016/S0921-8890(99)00065-2

39. S. Yun, M. Schwager, D. Rus, in *Robotics Research*, C. Pradalier, R. Siegwart, G. Hirzinger, Eds. (Springer Tracts in Advanced Robotics, vol. 70, Springer, 2011), pp. 607–623.

40. K. N. Nordstrom, J. P. Gollub, D. J. Durian, Dynamical heterogeneity in soft-particle suspensions under shear. *Phys. Rev. E Stat. Nonlin. Soft Matter Phys.* **84**, 021403 (2011). doi:10.1103/PhysRevE.84.021403 Medline

41. Z. Jiang, Q. Kemao, H. Miao, J. Yang, L. Tang, Path-independent digital image correlation with high accuracy, speed and robustness. *Opt. Lasers Eng.* **65**, 93–102 (2015). doi:10.1016/j.optlaseng.2014.06.011